

The author(s) shown below used Federal funds provided by the U.S. Department of Justice and prepared the following final report:

Document Title: High-Power Compact Microwave Source for Vehicle Immobilization, Final Report

Author: Eureka Aerospace

Document No.: 236756

Date Received: November 2011

Award Number: 2004-IJ-CX-K044

This report has not been published by the U.S. Department of Justice. To provide better customer service, NCJRS has made this Federally-funded grant final report available electronically in addition to traditional paper copies.

Opinions or points of view expressed are those of the author(s) and do not necessarily reflect the official position or policies of the U.S. Department of Justice.

High-Power Compact Microwave Source for Vehicle Immobilization

FINAL REPORT

Submitted to:

U.S. Department of Justice
Office of Justice Programs
National Institute of Justice

**Solicitation Topic: Less-lethal Technologies (Vehicle Immobilization),
Fiscal Year 2004**

April 20, 2006

Eureka Aerospace
3452 East Foothill Blvd, Suite 528,
Pasadena California 91107-3160
Tel. 626. 844-6664; Fax. 626. 844-6665
e-mail: tatoian@EurekaAerospace.com

This project was supported by Award No. 2004-IJ-CX-K044 awarded by the National Institute of Justice, Office of Justice Programs, US Department of Justice. The opinions, findings, and conclusions or recommendations expressed in this publication/program/exhibition are those of the author(s) and do not necessarily reflect the views of the Department of Justice. NIJ defines publications as any planned, written, visual or sound material substantively based on the project, formally prepared by the grant recipient for dissemination to the public.

Table of Contents

Abstract.....	3
1. Introduction.....	4
2. Analytical Developments.....	6
2.1 Microwave Oscillator.....	6
2.1.1 Quaterwave Oscillator-General Considerations	6
2.1.2. Ideal Case.....	8
2.1.3 Practical (Realistic) Case	12
2.2 Flare Horn Antenna Analysis.....	19
2.3 Spark Gap Switch Performance	22
3. Vulnerable Frequencies Test.....	23
4. Simulations	28
4.1 Finite Difference Time Domain (FDTD).....	28
4.2. Simulation Results	29
5. High-Power Electromagnetic System (HPEMS).....	32
5.1 Power Supply	33
5.2 Trigger Generation and Marx Generator	36
5.3. Blumlein Oscillator	37
5.4 Antenna	38
6. High-Power Microwave Experiments.....	39
6.1 Test Design and Test Configuration	39
6.2 Electric Field Measurements.....	39
6.3. Test Results	40
7. Summary.....	44

Abstract

Eureka Aerospace has developed a compact single frequency high-power electromagnetic system (HPEMS) for remotely immobilizing vehicles using microwave energy to disable/damage vehicle's electronic control module/microprocessor which controls engine's vital functions. The HPEMS consist of rapid charging power supply, capable of delivering of up to 100 pulses per second to the 16-stage Marx generator having erected voltage of 640 kV, whose output consist of 100 Joule, 50 ns long DC pulses. The Marx generator "feeds" the microwave oscillator, consisting of two-transmission line flat-plate Blumlein architecture converting DC pulses into RF-modulated waveform at 350 MHz, using a multiple spark-gap switch configuration. The extension of Blumlein and ground plates into flare horn geometry offers a unique oscillator-high-gain antenna configuration yielding focusing of microwave energy along the focal axis of the antenna. The measured electric field strength at the 30 ft range is approximately 60 kV/m, which corresponds to the power density of 477 W/cm². The limited laboratory test successfully demonstrated the system's capability of "killing" of the 1999 Honda Accord's engine with a single pulse at 35 ft range. More tests against many other vehicles and different geometric and radiometric parameters including range, aspect angle, frequency, pulse repetition frequency, and dwell are necessary for a comprehensive assessment of the system performance.

In addition, Eureka Aerospace carried out a series of laboratory tests to determine vehicle's "vulnerable" frequencies by examining the frequency response of the key electronic control module/ microprocessor's circuits/pins associated with the vital engine functions such as ignition control, ignition switch, fuel pump control etc. The "vulnerable" frequency tests against six different vehicles yielded a bank of vulnerable frequencies in the 200-1350 MHz range. We believe that using the vulnerable frequencies will allow for the development of an optimal system with significant reduction of power levels and aperture size. More tests are needed against many other cars (different manufacturers, different models, and different years). Moreover, additional tests against two or more identical vehicles are needed to assess the consistency of the results.

The HPEMS is capable of (1) high-value asset perimeter protection (Non-lethal area denial to vehicles) from approaching hostile vehicles, (2) bringing cars to a halt on urban, suburban and multi-lane highways, (3) perimeter protection for gas-oil (fueling) platforms at sea and (4) day/night all-weather clandestine operations. The potential host platforms for HPEMS include ground vehicle, helicopter or UAV. The HPEMS can be utilized in law enforcement, homeland security and applications such as counter-terrorism activities.

1. Introduction

There is a great interest in a narrowband, wideband and ultra-wideband electromagnetic sources for variety of applications including communications, ground penetrating radar and, recently, particularly electronic warfare [1]-[4]. Many varieties of sources have been developed to generate high power microwaves. These include klystrons, magnetrons, gyrotrons, vircators, ubitrons and beam plasma devices. Most microwave sources generate microwaves by converting the kinetic energy of electrons, thus wave-particle interaction is the basic physical mechanism for high power microwave generation.

The above mentioned sources require high-voltage, high-power pulse sources. Existing pulse power sources can deliver up to megajoules of energy, hundreds of thousands of amperes of current or terawatts of power. The associated pulse widths vary from microseconds for the highest power levels to several seconds for highest energy levels. Since many sources can operate in high-power regimes (sometimes in CW regime) it follows that they can deliver huge average powers. In a typical source the first stage consists of multi-stage Marx generator with several capacitors that are charged in parallel and discharged in series by breakdown switches which produces high-voltage output. Due to the internal parasitic inductance, the output of a Marx generator, generally speaking, will have a relatively slow rise time. In order to decrease the rise time, a Blumlein configuration with a breakdown switch is used. By filling the Blumlein with water one can increase the capacitance significantly and the resulting capacitors can be store more energy. For a Blumlein in a coaxial configuration, the internal inductance is quite small, resulting in a very fast rise time for the output pulse.

Used in weapon-like applications, high-power microwave systems can disrupt or damage electronic components of a target by inducing large parasitic currents in wires that are connected to the electronic module control/microprocessors. The damage occurs due to the dielectric breakdown or chip-to-etch wire melting. The dielectric breakdown requires large peak voltages or electric fields, while chip-to-etch wire melting occurs due to large average power. For example, it can be shown that tens of amperes are needed to melt chip-to-etch wires made of gold or copper.

Unfortunately, pulse power sources for high power microwave sources tend to be bulky and heavy and not suitable for applications requiring a compact and lightweight system. The alternative approach for generating high-power microwaves is to use damped sinewave oscillators such as quarter-wave transmission line (to be discussed later) driven by Marx generator. These oscillators convert Marx-generated DC pulses into microwaves. Loaded by a suitable antenna, such systems are shown to be effective in some practical applications. The main drawback of such system is that the generated waveforms contain limited number of cycles and they are not tunable for wide range of frequencies. Moreover, because of the limitations associated with spark-gap switches and insulating media, such systems are shown to operate in a relatively low (few hundred Hz) pulse repetition frequency (PRF) modes. While the achievable peak radiated power can be in gigawatt range, the limitations on radiated pulsewidth (small number of cycles)

and PRF implies significantly low average power compared to microwave sources such as gyrotrons, vircators etc. Moreover, the relatively low Q results in fast damping of the waveforms resulting in only a few cycles which in turn, limits the system efficiency as a weapon. For a microwave weapon to be efficient, the Q of the source must exceed the Q of the target's circuitry. The quality factor Q of the source is given by $\pi \times N$, where N is the number of cycles it takes for the amplitude of the radiated field to fall from peak to $(1/e)$ or 36% value. Typically, the source Q needs to be in the range of 10 to 20, so that it is higher than the target Q , for efficient coupling.

Very recently experimental results of a resonant Blumlein pulser configuration operating in 15-30 kV and tunable in the important parameters of pulsewidth, bandwidth and center frequency are reported by researchers at University of New Mexico and ASR [5]. The researchers utilized parallel plate Blumlein architecture to create a tunable pulser. Their strategy relies on the parasitic impedances and the imbalance in impedance that occurs during the displacement of the center conductor in the parallel Blumlein topology. The pulser was designed to operate in the 300 MHz-2 GHz range. Moreover, the authors report the design of a compact hydrogen switch with rise time less than 200 ps at charge voltage of 15 kV.

In their study of the an ultra-wideband source using gallium arsenide photoconductive semiconductor switches [6], at a relatively low power levels, the researchers investigated both the parallel plate and coaxial Blumlein configurations for microwave generations. The results suggest there can be significant coupling of the two transmission lines through electric fields instead of currents that can be included as parasitic impedance, which ultimately has a degrading effect on Blumlein performance. The degradation exhibited by the reduction of output pulse amplitude and some ringing effect. The authors suggest that by stacking multiple Blumleins one can reduce the parasitic coupling terms.

DIEHL Gmbh, based in Germany, has developed a series of microwave sources, based on multi-stage Marx generators and microwave oscillators (method of generating microwaves from DC pulses is unclear) ranging from man portable [DS110 operating at 375 MHz and DS110B operating at 100-300 MHz range], and stationary unit [Model DS350 operating at 100 MHz (in oil), 60 MHz (in glycol) and 50 MHz (in water)-all at maximum PRF of 50 Hz]. The man portable systems reportedly generate 400 kV (DS110) and 700 kV (DS110B), while the stationary unit output can achieve 1MV. While the author reports 30-min continuous operation, all of the models have very low Q , where the number of cycles does not exceed three [7]. Moreover, both the portable and stationary systems use a single dipole-like rod—an omni-directional radiator. The recent private conversation with Mr. Bohl—a member of the DIEHL's technical staff—indicates that they are working on the development/implementation of a high-gain antenna to improve the efficiency of the above systems to be used in military applications.

A large high-voltage transient (impulse) system built at the Air Force Research Laboratory (AFRL) during 1997-1999 [8], where the pulse power centers on the compact transformer capable of generating 1 MV at 600 Hz PRF. The load consist of a 4-m

diameter 85 Ohm half impulse radiating antenna (half IRA) that can deliver a far radiated field with a rise time of nearly 80 ps and a field-range product (rE_{far}) of ~ 6 MV! While such a transient system can generate huge peak power, its instantaneous bandwidth is very large so that the power densities at individual frequencies are relatively low and thus, we believe, is not very effective for weapon-like applications.

A series of tests were carried out by ARL using powerful but bulky and heavy military surplus microwave generating equipment, where single frequencies varied between 1.25 GHz and 5 GHz against a variety of vehicles [9]. The results showed that the disruption/age of electronic modules occurs at the field levels, at the vehicle site, in excess of 10 kV/m, which corresponds to the power density of 26 W/cm². The concept of tunability of the source applied to flat-plate Blumlein source architecture and its applications for disrupting vehicles' vital engine functions is first discussed by Eureka Aerospace [10].

Finally, we must emphasize that a comprehensive review of all the technologies for terminating vehicle pursuits, directly related to the problem at hand, performance and operational assessments, safety and security assessment, assessment of public acceptance and privacy issues, assessment of public and private costs is discussed in the report by Helmick [11]. The report covers broad range of technologies including mechanical, chemical, electrical (direct injection and so-called radiative devices that radiate electromagnetic energy into the fleeing vehicle to destroy vehicle's engine control systems), sensory and cooperative. In particular, the author emphasizes that the radiative devices "appear to have significant promise for use in typical police pursuits" according to the Pursuit Management Task Force (PMTF) and that there is potential for these devices to be effective tools for law enforcement. Moreover, the PMTF recommends that radiative electromagnetic systems, including high-power microwaves and retractable direct injection systems be identified as high priority and moved quickly and aggressively to prototype stages for the evaluation. An excellent overview of the PMTF effort is summarized in the Executive Summary Report [12].

2. Analytical Developments

2.1 Microwave Oscillator

The oscillator constitutes, perhaps, the most important element of the entire HPEMS. It converts the DC power into microwave power using a two-transmission lines Blumlein configuration, which is essentially a quarter-wavelength resonator.

2.1.1 Quarter Wave Oscillator-General Considerations

In order to understand the operational principle of the quarter wave microwave oscillator utilizing two transmission line Blumlein configuration, first let us consider a single quarter-wave transmission line oscillator with the nonlinear element consisting of a

spark-gap switch immersed in dielectric medium such as oil and its equivalent electrical circuit: (see Figs.1 and 2). Here the transmission line is differentially charged to $v_0 f(t)$, where $f(t)$ is a unit step function. Its transform is $v_0 \hat{f}(s)$, where the complex frequency $s = \Omega + i\omega$ and the propagation constant in oil is give by:

$$\zeta = \frac{s}{c_0} = \frac{\Omega + i\omega}{c_0} = \frac{\Omega}{c_0} + ik_0$$

where k_0 is the wavenumber.

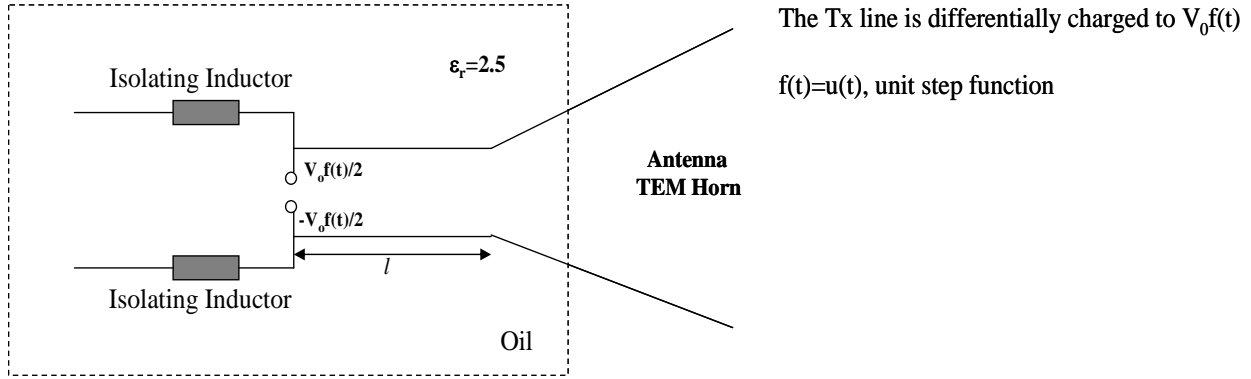


Figure.1. Quarter wave oscillator.

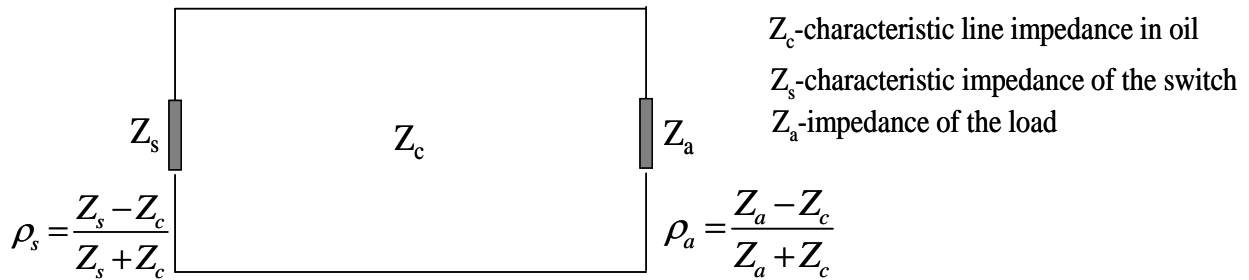


Figure 2. Quarter wave oscillator equivalent circuit.

Reflection coefficients at the switch and antenna load are respectively:

$$\rho_s = \frac{Z_s - Z_c}{Z_s + Z_c} \qquad \rho_a = \frac{Z_a - Z_c}{Z_a + Z_c}$$

Ideally (ideal switch), $Z_s=0$ implying $\rho = -1$. The general solution for the voltage and current along the transmission line (coordinate z) is given by

$$\begin{aligned}\widehat{V}(z) &= Ae^{-\zeta z} + Be^{\zeta z} \\ \widehat{I}(z) &= \frac{A}{Z_c}e^{-\zeta z} - \frac{B}{Z_c}e^{\zeta z}\end{aligned}\quad (1)$$

The boundary conditions (BC) are:

$$\begin{aligned}V(0) &= -v_0\widehat{f}(s) - I(0)Z_s \\ V(l) &= Z_a I(l)\end{aligned}\quad (2)$$

Applying the BC implies

$$\begin{aligned}A &= \frac{B}{\rho_a}e^{2\zeta l} \\ \text{and } B &= -v_0\widehat{f}(s)\frac{Z_c}{Z_c + Z_s}\frac{\rho_a}{e^{2\zeta l} - \rho_a\rho_s}\end{aligned}\quad (3)$$

We are interested in $V(l)$ -voltage into antenna.

$$\widehat{V}(l) = Ae^{-\zeta l} + Be^{\zeta l} = \frac{B}{\rho_a}e^{\zeta l} + Be^{\zeta l} = Be^{\zeta l}\left[\frac{1}{\rho_a} + 1\right],$$

which can be rewritten as

$$\widehat{V}(l) = -v_0\widehat{f}(s)\frac{Z_c}{Z_c + Z_s}\frac{e^{\zeta l}(1 + \rho_a)}{e^{2\zeta l} - \rho_a\rho_s}$$

and further we have

$$\widehat{V}(l) = -v_0\widehat{f}(s)\frac{Z_c}{Z_c + Z_s}\frac{e^{-\zeta l}(1 + \rho_a)}{1 - \rho_a\rho_s e^{-2\zeta l}}\quad (4a)$$

the normalized form of which becomes

$$\frac{\widehat{V}(l)}{v_0} = -\widehat{f}(s)\frac{Z_c}{Z_c + Z_s}\frac{e^{-\zeta l}(1 + \rho_a)}{1 - \rho_a\rho_s e^{-2\zeta l}}\quad (4b)$$

2.1.2 Ideal Case

Let's assume the following ideal conditions:

1. Ideal switch $Z_s=0$; $\rho_s = -1$

2. Ideal step function charging: $f(t)=u(t)$, implying $\hat{f}(s) = \frac{1}{s}$.

It follows that,

$$\begin{aligned} \frac{\hat{V}(l)}{v_0} &= -\frac{v_0}{s} \frac{e^{-\zeta l} (1 + \rho_a)}{1 + \rho_a e^{-2\zeta l}} \\ &= -\frac{v_0}{s} (1 + \rho_a) e^{-\zeta l} [1 - \rho_a e^{-2\zeta l} + \rho_a^2 e^{-4\zeta l} - \dots] \\ &= -\frac{v_0}{s} (1 + \rho_a) [1 - \rho_a e^{-3\zeta l} + \rho_a^2 e^{-5\zeta l} - \dots] \end{aligned} \quad (5)$$

Inverse transformation yields:

$$V(t) = -v_0 (1 + \rho_a) \left[u\left(t - \frac{l}{c_0}\right) - \rho_a u\left(t - \frac{3l}{c_0}\right) + \rho_a^2 u\left(t - \frac{5l}{c_0}\right) - \dots \right] \quad (6)$$

The total normalized voltage is:

$$\begin{aligned} V(l,t) &= \frac{v_0 + V(t)}{v_0} = 1 + \frac{V(t)}{v_0} \\ &= 1 - (1 + \rho_a) \left[u\left(t - \frac{l}{c_0}\right) - \rho_a u\left(t - \frac{3l}{c_0}\right) + \rho_a^2 u\left(t - \frac{5l}{c_0}\right) - \dots \right] \end{aligned} \quad (7)$$

and

$$\frac{V(t)}{v_0} = -(1 + \rho_a) \left[u\left(t - \frac{l}{c_0}\right) - \rho_a u\left(t - \frac{3l}{c_0}\right) + \rho_a^2 u\left(t - \frac{5l}{c_0}\right) - \dots \right] \quad (8)$$

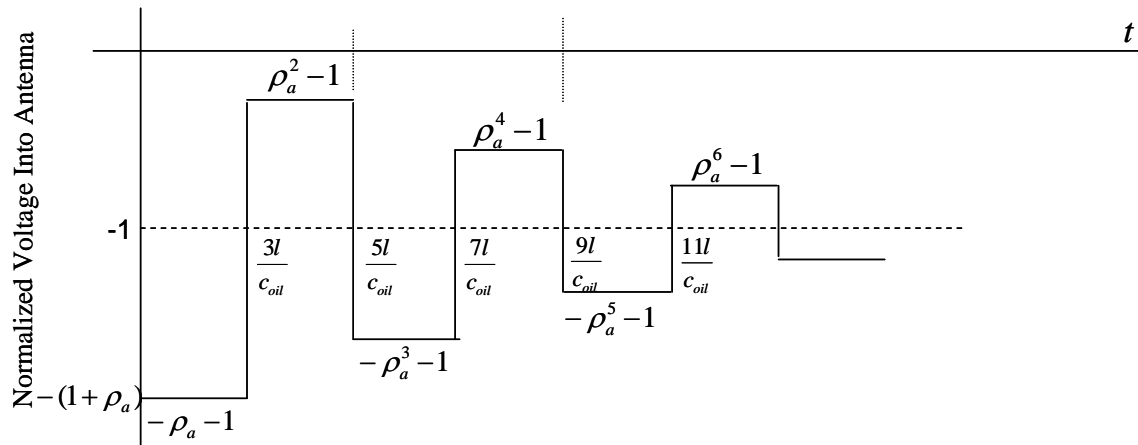


Figure 3a. Voltage into antenna $[V(t)/v_0]$.

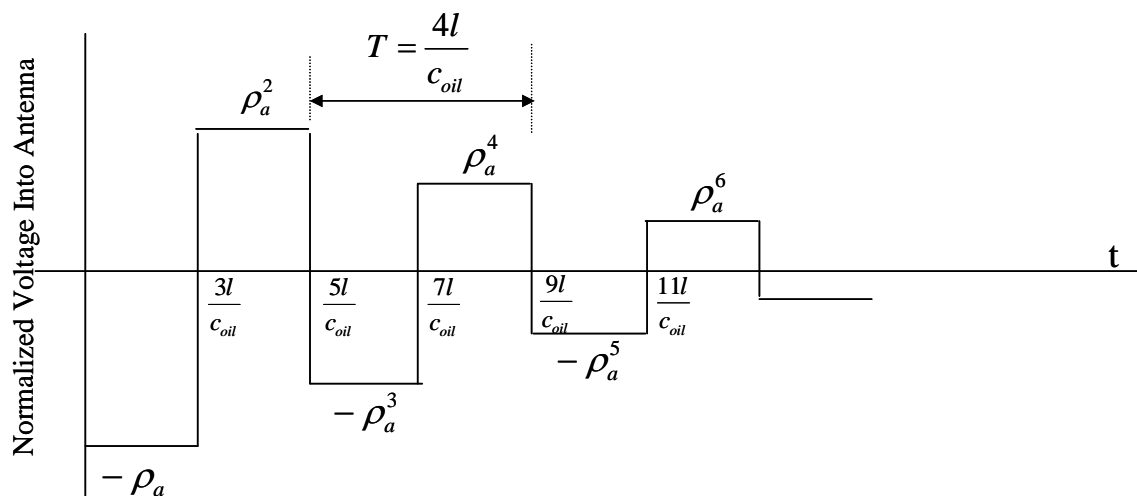


Figure 3b. Normalized voltage into antenna $[\frac{v_0 + V(t)}{v_0}]$.

For example, $R=100$ Ohm and $Z_c=10$ Ohm yields $\rho_a = \frac{100-10}{100+10} = 0.818$. Thus, $\rho_a^2 = 0.669$, $\rho_a^3 = 0.547$, $\rho_a^4 = 0.448$ etc.

If the pulse charge up has a finite rise, instead of square pulses we'll have a damped sinusoid as shown in Fig.4.

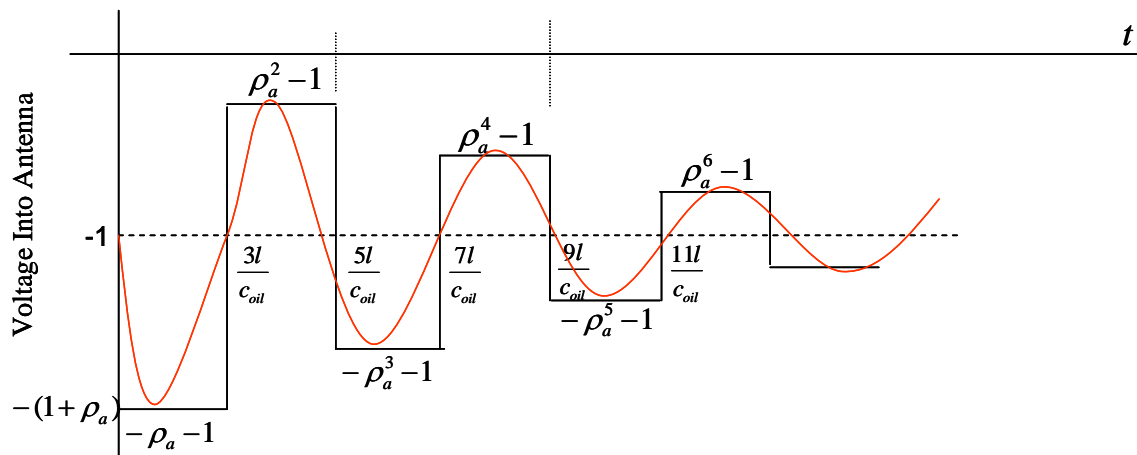


Fig. 4. Damped oscillations (red curve) due to finite rise of the charging voltage.

The functional form of the voltage is

$$V(l, t) = -\rho_a \sin(\omega_0 t) e^{-\frac{\omega_0 t}{2Q}}$$

where

$$Q = \frac{-\pi}{2 \ln \rho_a} = \pi N$$

and N is the number of cycles for a fall in amplitude by a factor $1/e$. The amplitude drops in the following manner:

In 1 cycle, ρ_a is reduced to ρ_a^3 implying the reduction ratio of ρ_a^2 .

In 2 cycles, ρ_a is reduced to ρ_a^5 implying the reduction ratio of ρ_a^4 .

In 3 cycle, ρ_a is reduced to ρ_a^7 implying the reduction ratio of ρ_a^6 .

In N cycle, ρ_a is reduced to $\rho_a^{(2N+1)}$ implying the reduction ratio of ρ_a^{2N} .

Solving $\rho_a^{2N} = e^{-1}$ for N gives

$$N = -\frac{1}{2 \ln(\rho_a)}$$

It can be shown that

$$N = -\frac{1}{2 \ln\left[\frac{R_a - Z_c}{R_a + Z_c}\right]} = \frac{1}{2 \ln\left[\frac{R_a + Z_c}{R_a - Z_c}\right]} = \frac{1}{2 \ln\left[\frac{1 + \beta}{1 - \beta}\right]} \quad (9)$$

where

$$\beta = \frac{Z_c}{R_a} \quad 1 \leq \beta \leq 1$$

Equivalently,

$$e^{-\pi N/Q} = \rho_a^{2N}$$

implying

$$Q = \frac{-\pi}{2 \ln \rho_a} = \pi N$$

which shows very convenient expression for the Q of the oscillator in terms of number of cycles. For example, if $\beta=1$ ($R_a=100$ Ohm, $Z_c=10$ Ohm), it follows that $N \sim 2.492$ and $Q=7.828$.

The damped sinusoidal output is

$$\begin{aligned} \frac{V(l,t)}{v_0} &\approx - \left[1 + \rho_a \sin(\omega_0 t) e^{\frac{-\omega_0 t}{2Q}} \right] \\ &= - \left[1 + \rho_a \sin(2\pi f_0 t) e^{2f_0 t \ln(\rho_a)} \right] \end{aligned} \quad (10)$$

Equivalently,

$$\frac{V(l,t)}{v_0} = - \left[1 + \left(\frac{1-\beta}{1+\beta} \right) \sin(2\pi f_0 t) e^{-2f_0 t \ln\left(\frac{1+\beta}{1-\beta}\right)} \right]$$

2.1.3. Practical (Realistic) Case

Before we proceed to discussion of the realistic switch case, we'd like to make few observations. First of all we should state that that parameter Z_s consist of both the resistive and inductive components, namely, $Z_s = R_s + i\omega L_s$. The reflection coefficient at the switch is:

$$\rho_s = \frac{Z_s - Z_c}{Z_s + Z_c} = \frac{i\omega L_s - Z_c}{i\omega L_s + Z_c}$$

Since the inductance of the transmission line, L_l , is

$$L_l = L_l l$$

where L_l is the inductance per unit length and l is the length of the transmission line, and since it can also be expressed via the transition time time, t_r of the signal,

$$L_l = Z_c t_r$$

it follows that

$$Z_c = \frac{L_l}{t_r} = \frac{L_l c_{oil}}{l}$$

Consequently,

$$\rho_s = \left[\frac{i\omega \frac{L_s}{L_l} - \frac{1}{t_r}}{i\omega \frac{L_s}{L_l} + \frac{1}{t_r}} \right] = \frac{i\omega\alpha - \frac{1}{t_r}}{i\omega\alpha + \frac{1}{t_r}} \quad (11)$$

where

$$\alpha = \frac{L_s}{L_l}$$

is a parameter that describes the ratio of switch inductance to the line inductance.

Furthermore, from

$$\rho_s = \frac{Z_s - R_c}{Z_s + R_c}$$

it follows that

$$\frac{1}{|\rho_s|} = \frac{Z_c + R_s}{Z_c - R_s} = \frac{1 + \frac{R_s}{Z_c}}{1 - \frac{R_s}{Z_c}} = \frac{1 + \delta}{1 - \delta} \quad (12)$$

where

$$\delta = \frac{R_s}{Z_c}$$

To maximize the output we need to minimize the denominator in Eq.(4b), namely:

$$\rho_a \rho_s e^{\frac{-2\zeta l}{c}} = 1.$$

This implies that

$$s_n \frac{2l}{c} = \ln[\rho_a |\rho_s|] + i\pi n \quad n = 0, 2, 4, \dots$$

Clearly,

$$s_1 = -\frac{c}{2l} \left\{ \ln\left(\frac{1}{\rho_a}\right) + \ln\left(\frac{1}{|\rho_s|}\right) \right\} + i \frac{c\pi}{2l}$$

Therefore,

$$\frac{1}{Q} = \frac{2}{\pi} \left\{ \ln\left(\frac{1}{\rho_a}\right) + \ln\left(\frac{1}{|\rho_s|}\right) \right\} = \frac{2}{\pi} \left\{ \ln\left(\frac{1+\beta}{1-\beta}\right) + \ln\left(\frac{1+\delta}{1-\delta}\right) \right\}$$

which implies that

$$Q = \frac{\pi}{2 \left[\ln\left(\frac{1+\beta}{1-\beta}\right) + \ln\left(\frac{1+\delta}{1-\delta}\right) \right]}. \quad (13)$$

Where the percent bandwidth is defines as follows:

$$\text{percentbandwidth} = \frac{100}{Q} = \frac{200}{\pi} \left[\ln\left(\frac{1+\beta}{1-\beta}\right) + \ln\left(\frac{1+\delta}{1-\delta}\right) \right]$$

Finally, substituting Q from Eq. (13) into Eq.(10) yields the final expression for the normalized voltage on the load:

$$\frac{V(l, t)}{v_0} \approx - \left[1 + \rho_a \sin(2\pi f_0 t) e^{\frac{-2\pi f_0 t}{2Q(\beta, \delta)}} \right] \quad (14)$$

Figs. 5-7 depict various illustrative examples with different parameters β and δ - all obtained using the above Eq. (14). This can be used as a valuable tool/model for synthesizing the desired waveform and determining the key switch and transmission line parameters that can support it.

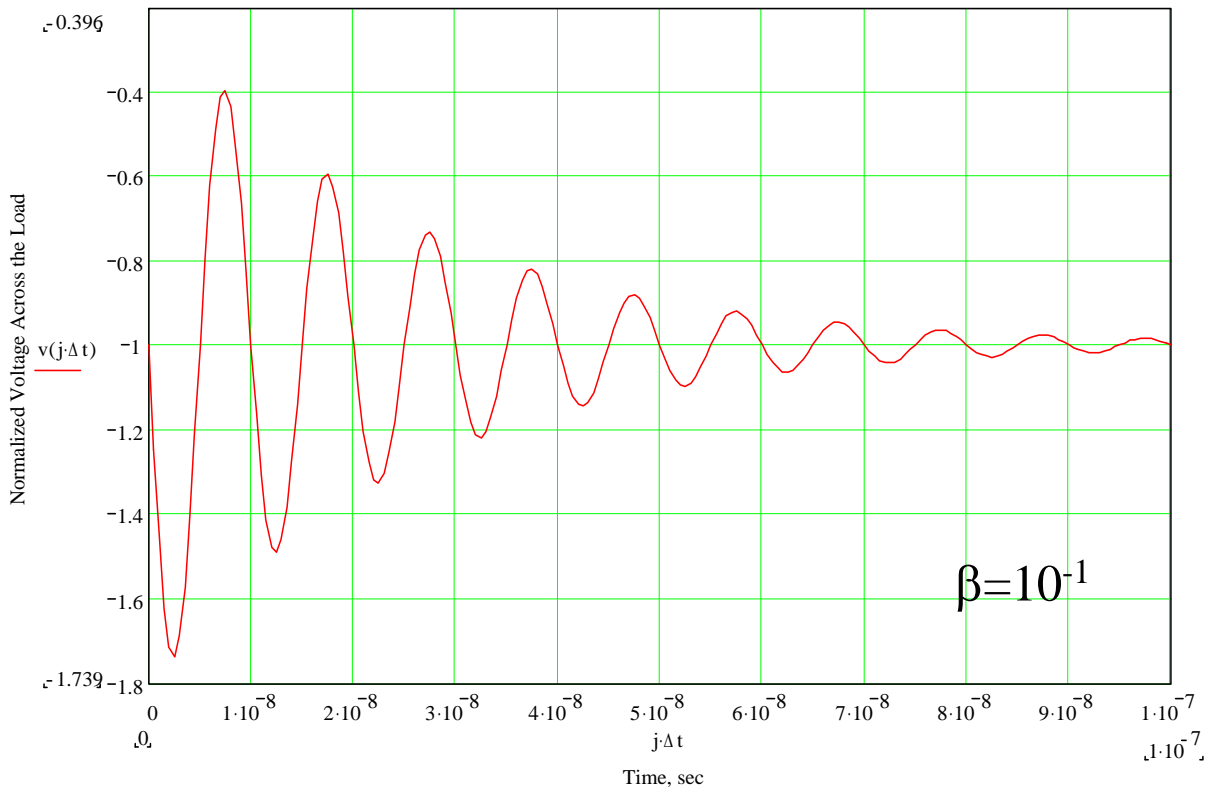
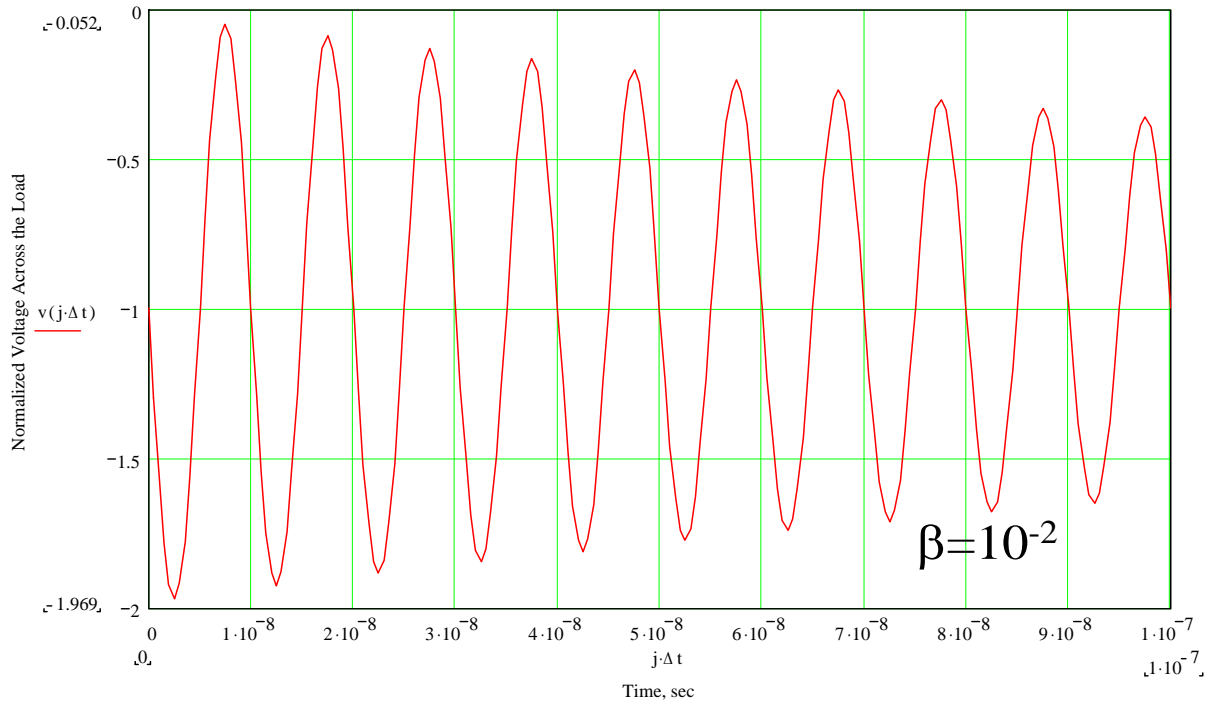


Fig.5. Normalized Voltage Across the Load at 100 MHz ($\delta=10^{-3}$).

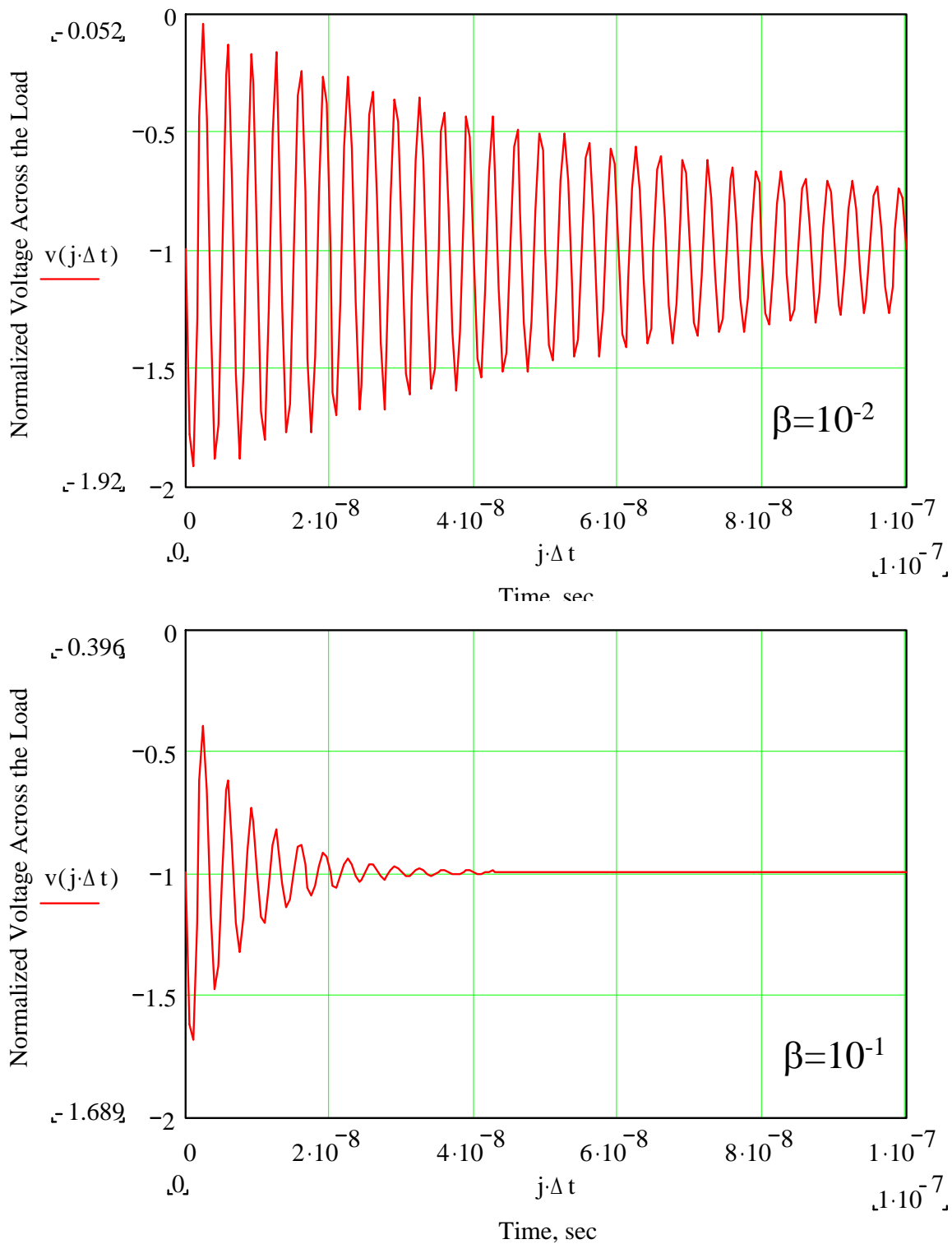


Fig.6. Normalized Voltage Across the Load at 300 MHz ($\delta=10^{-3}$).

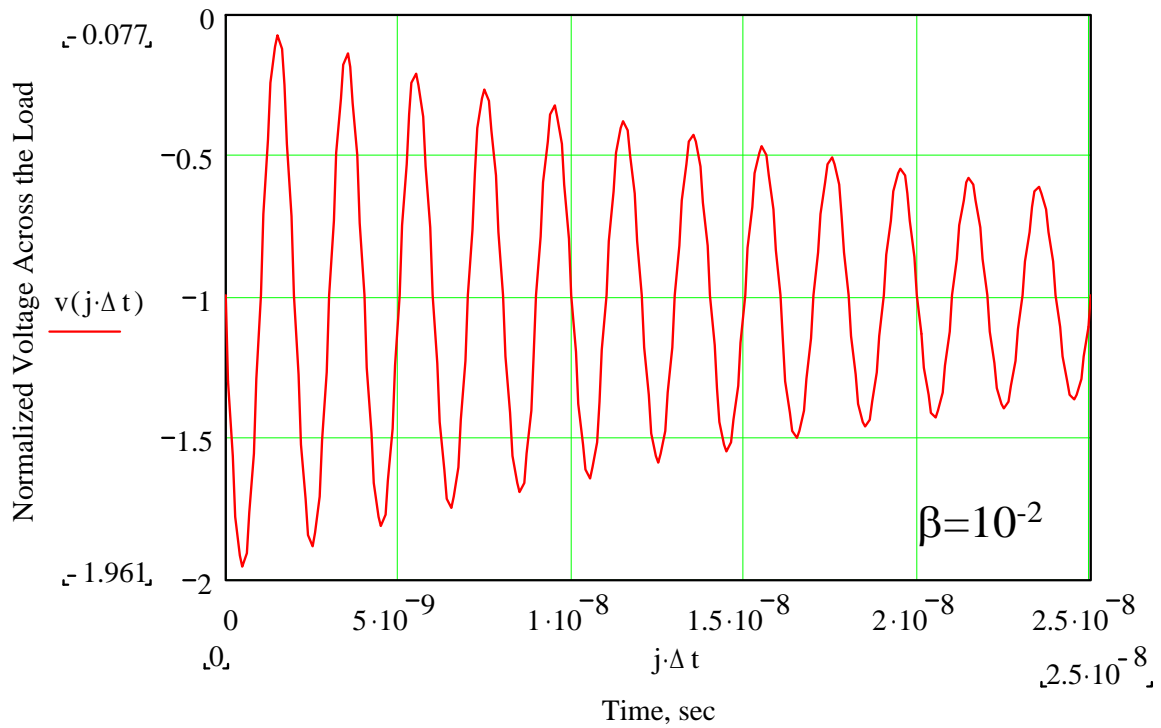
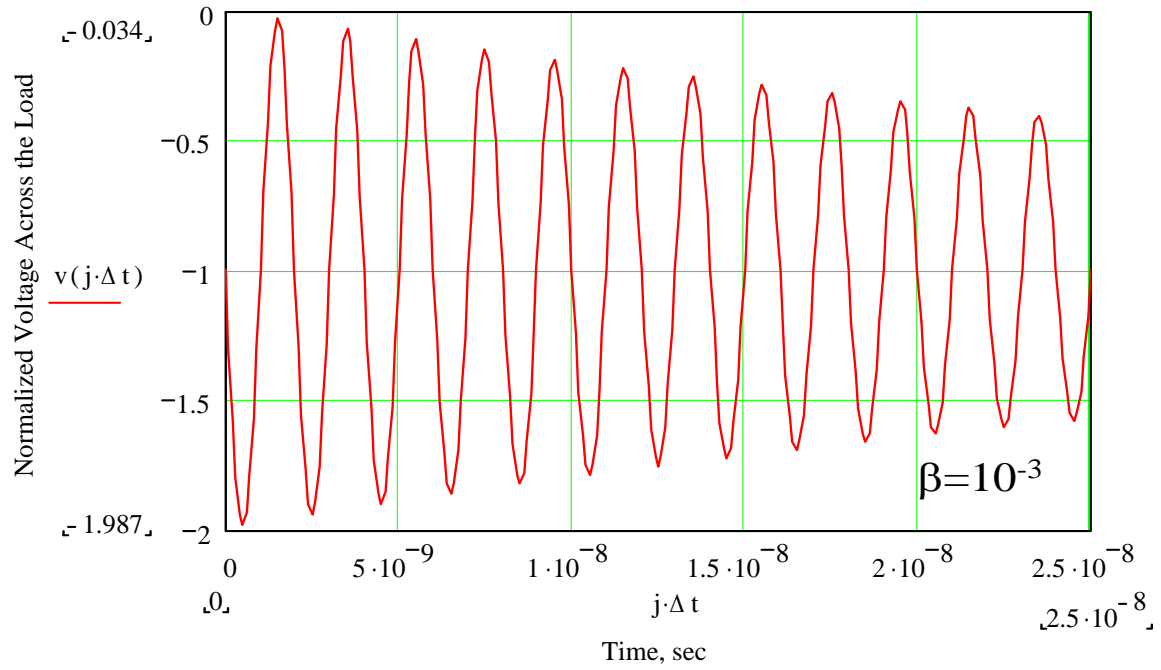


Fig. 7. Normalized Voltage Across the Load at 500 MHz ($\delta = 10^{-2}$).

2.2 Flare Horn Antenna Analysis

Here are my latest predictions for horn gains. The approximations involved require that the horn throat angles not be too large. For half-angles no larger than 45 degrees, the formulas should give reasonable accuracy. However, no VSWR effects are included here, and can be substantial.

The prompt response of an unfocused circularly conical TEM horn is given by

$$E = 1.07V \frac{\sqrt{\frac{Y+1}{Y-1}}}{4r}$$

$$Y = \sqrt{1 + \left(\frac{D}{2F}\right)^2}$$

where E is the electric field at distance r on boresight, D is the diameter, and F is the length or focal length, and V is the applied Voltage. This expression includes the stereographic projection correction. The prompt response holds only for the clear time dt , which in the far field on boresight is given by

$$dt = \left[\sqrt{1 + \left(\frac{D}{2F}\right)^2} - 1 \right] \frac{F}{c}$$

where c is the speed of light. After this clear time the step response is rather small for small angle horns and can be neglected for our purposes here.

When driven by a sinusoidal signal, these horns have the highest gain when the clear time is half of the rf period. In the far field on boresight this requires that

$$\frac{\lambda}{2} = \left[\sqrt{1 + \left(\frac{D}{2F}\right)^2} - 1 \right] F$$

or

$$D = \lambda \sqrt{1 + \frac{4F}{\lambda}}$$

or

$$F = \lambda \frac{\left[\left(\frac{D}{\lambda} \right)^2 - 1 \right]}{4}$$

where λ is the wavelength. Constrained by the above equation, the field E_1 at distance r on boresight in the far field is twice that of the antenna's prompt response when driven by a narrow band signal, and is given by

$$E_1 = 1.07V \frac{\sqrt{1 + \frac{4F}{\lambda}}}{2r} = 1.07V \frac{D}{2\lambda r}$$

The signal strengths on bore sight should be similar for all odd harmonics as well.

The same horn antenna with a proper focusing optic has a radiated field given by

$$E_2 = 1.07\pi V \frac{D}{4\lambda r}$$

The ratio of the responses given by the above two equations is simply

$$\frac{E_1}{E_2} = \frac{2}{\pi}$$

Consider a diameter $D=2\lambda$ and length $F=0.75\lambda$. Then we have ,

$$\text{Horn Alone: } E_1 = 1.07V \frac{D}{2\lambda r} = 1.07 \frac{V}{r}$$

$$\text{Horn \& Lens: } E_2 = 1.07\pi V \frac{D}{4\lambda r} = 1.68 \frac{V}{r}$$

Consider a diameter $D=3\lambda$ and length $F=2\lambda$. Then we have,

$$\text{Horn Alone: } E_1 = 1.07V \frac{D}{2\lambda r} = 1.60 \frac{V}{r}$$

$$\text{Horn \& Lens: } E_2 = 1.07\pi V \frac{D}{4\lambda r} = 2.52 \frac{V}{r}$$

Consider a diameter $D=4\lambda$ and length $F=3.75\lambda$. Then we have,

$$\text{Horn Alone: } E_1 = 1.07V \frac{D}{2\lambda r} = 2.14 \frac{V}{r}$$

$$\text{Horn \& Lens: } E_2 = 1.07\pi V \frac{D}{4\lambda r} = 3.36 \frac{V}{r}$$

Consider a diameter $D=6\lambda$ and length $F=8.75\lambda$. Then we have,

$$\text{Horn Alone: } E_1 = 1.07V \frac{D}{2\lambda r} = 3.21 \frac{V}{r}$$

$$\text{Horn \& Lens: } E_2 = 1.07\pi V \frac{D}{4\lambda r} = 5.04 \frac{V}{r}$$

The field from the unfocused optimized horn is $2/\pi$ or 63.7% of the focused horn. A lens would be unreasonably heavy. Thus a reflector antenna would be preferred. However, the reduced aperture efficiency of reflector IRA antenna would give a radiated field of 74% to 85% of a focused horn antenna with the same aperture size. However, there are better ways to feed a reflector antenna with narrow-band signals. Very large systems like the VLA achieve aperture efficiencies of 65%, which would give radiated fields of 80% of the maximum theoretically possible. This is to be compared with a reflector IRA at 50 to 57%, the circularly conical TEM horn at 42.2%, and the lens IRA at 67.8%. Smaller reflector antennas will be less efficient due to aperture blockage.

The table below summarizes these results.

	<u>Aperture Efficiency</u>	<u>Field Amplitude Ratio</u>
TEM Horn	--	42.2%
Reflector IRA	25% - 33%	50% - 57.4%
Lens-Horn IRA	46%	67.8%
VLA Dish	65%	80.6%

2.3 Spark-Gap Switch Performance

Several cycles of the unloaded output of a charged quarter-wave transmission line shorted at one end by a Braginskii-model spark switch are shown in Fig. 8 below. Here we use the risetime τ' defined by the maximum slope in the waveform, defined by the maximum rate of change in voltage into equivalent real impedance. In this case that would be a long transmission line of the same impedance.

$$\tau' = \frac{\max V}{\max\left(\frac{dV}{dt}\right)}$$

Harmonic generation is apparent. The major switch loss occurs at early time. The need for a fast switch is clear. The system should be optimized around the expected switch performance before a final design is established. Other switch models are available.

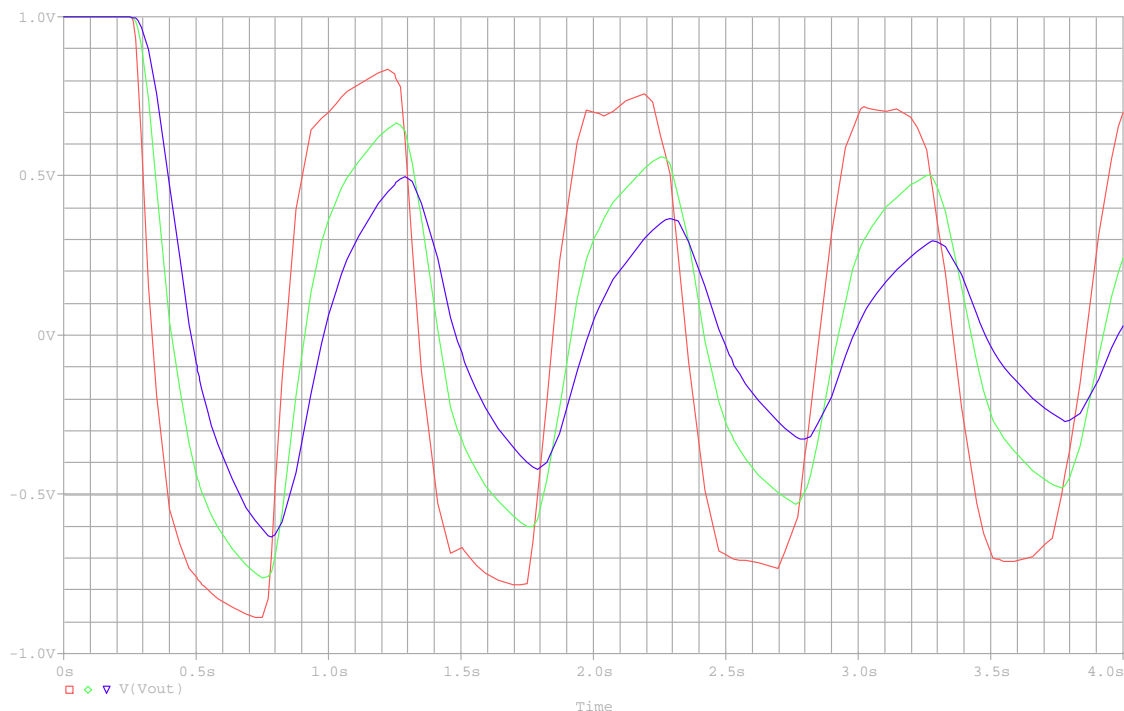


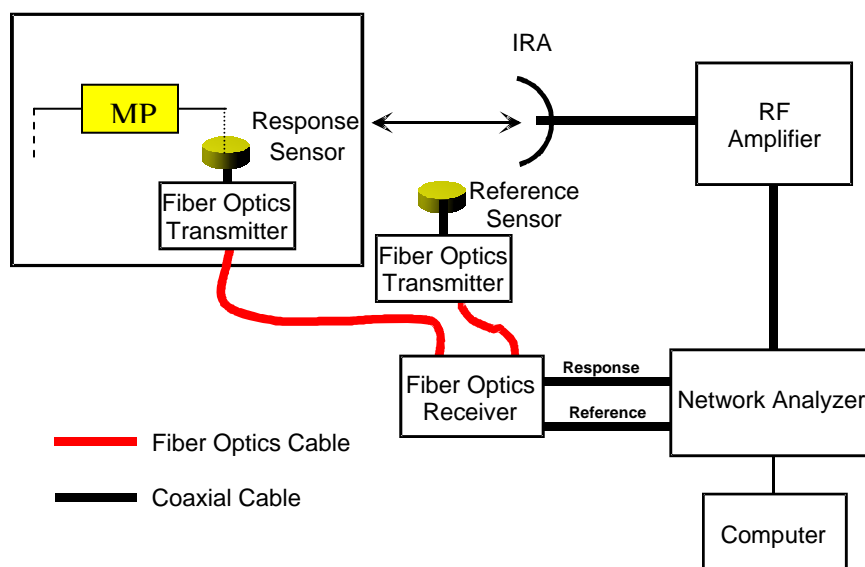
Figure 8. Relative output voltage V/V_0 versus relative time $f_0 t$ for several cycles of a charged quarter-wave transmission line shorted at one end by a Braginskii spark switch. The switch risetime parameters for the three curves are given by $f_0 \tau' = 0.1, 0.2, \text{ and } 0.3$, where f_0 is the natural oscillation frequency of the shorted quarter-wave line. The 10% to 90% risetime for a Braginskii arc switch is $\tau_{10} = 2.54\tau'$.

Clearly, good switch performance is achieved when $f_0 \tau' \ll 1$.

3. Vulnerable Frequencies Tests

The key objective of this task was to execute series of tests using pre-selected series of MPs associated with specific vehicles including key US and foreign manufacturers such as Ford, GM, Chrysler Daimler, Toyota, Nissan and Honda in order to assess the most “vulnerable” MP frequencies, which will lead to the optimal HPEMS design. After brief reconfirmation of the preliminary test design and setup, all the selected hardware/instrumentation will be acquired to carry out MP “frequency vulnerability tests.

The tests commenced with calibration of all equipment/instruments and the ambient environment. Then, Eureka Aerospace executed series of tests on the actual vehicles where the evaluation and assessment of the results will be done in both time and frequency domains. Eureka Aerospace carried out a systematic study of the frequencies in the 300MHz-1.4 GHz for a narrow-band HPEMS. The effort consisted of using the Network Analyzer (NA) in the swept CW mode to generate narrow-band signals spanning 300 MHz-1.4 GHz range in 100 KHz steps (see Fig. 9, top). The generated signals were radiated by Eureka’s 46-cm Impulse Radiating Antenna (IRA) [here the IRA operated in a narrow-band regime]. The oscillator in the NA puts out only milliwatts of power. The NA is then followed by a power amplifier with a nearly flat broadband gain. So, several watts or hundreds of watts goes into the IRA. The variation in gain of the power amplifier is a non-issue, since the NA plots measured response divided by the input voltage or power. It is truly a transfer function measurement. The IRA was placed near the test microprocessor. The “parasitic” currents (interference), induced in the MP wire(s) were measured for their frequency content at each exposure frequency. The frequency at which microprocessor response function achieves its maximum and the associated Q s ($Q=f_v / \Delta f_v$), indicating strong coupling between incident radiation and electronic circuitry. The Q of the source should exceed the Q of the target for efficient coupling.



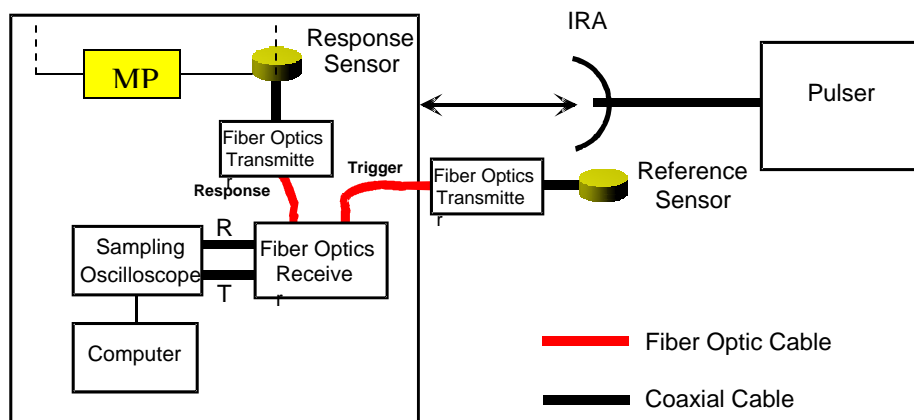


Figure 9. Equipment configuration for MP CW (top) and transient (bottom) measurements.

Our preliminary choice for matrix NA was Agilent’s 8753E model covering 30 kHz to 3 GHz (optional to 6 GHz). It offers S-parameter test set with solid-state switching and has up to 110 dB dynamic range. Moreover it has built-in floppy drive for recording instrument states and acquired data. The S-parameter option is useful in characterizing the IRA at its input port. The output power is 100 mW and we’ll need a power amplifier for these frequencies.

For the transient measurements we also utilized the 46cm diameter IRA in the impulse regime, using 2.8 kV high power pulse source (HYPS) delivering 2 ns pulses with risetime of ~100 ps, which will produce impulse-like waveforms over localized portions of the automobile under test. It has the advantage of an extremely broadband spectrum ranging from 300 MHz to 3 GHz, the same as was already used during Eureka’s tests during the SBIR Phase I “Through-the-Wall” impulse radar measurement effort (March-April 2002). Note that the lower frequency limit is governed by the antenna size and the high frequency limit is a function of the rise-time of the pulser voltage fed into the antenna. The internal response measured in time domain on the wire bundle entering the critical MP will consist of useful information about the automobile across a broad range of frequencies. Initially, the incident fields radiated from the IRA are easily calculated using existing analytical formulations, with the knowledge of the antenna geometry, distance to automobile and the pulser details. The exact geometry of the transmitter and the automobile was somewhat unimportant at this time, since our interest was the transfer function measurements at low and non-destructive incident field and power levels. This radiating system is capable of producing sufficiently broadband environment for the automobile measurements. The pulse test method described here is a new concept, in the sense that it may have been discussed by researchers, but not performed on an

automobile. Tektronix TDS8000 digital sampling scope (having up to 50 GHz bandwidth), including Tektronix 80E01 Module, was used in these transient tests. Test configuration for transient regime measurements is shown in Fig. 9 (bottom).

The Prodyn’s IP-2-1 model current sensor was used throughout the experiments. This is a doughnut-shaped high frequency current sensor for measuring current on small conductors that can be passed through the center hole of the probe. The sensor has a single ended 50 Ω output with an SMA connector. The frequency range (3 dB points) for this sensor with a fairly flat response is 100 kHz to 1.3 GHz. The relationship between the sensed current I_s and output voltage V_{out} is given by $V_{out} = Z_t \times I_s$ where Z_t is the transfer impedance of the sensor. When operating in a circuit with a 50 Ω impedance level, the IP-2-10 sensor has a transfer impedance of 1 Ω. The maximum current the sensor can handle is 0.8 A. To get a 100 μV output from the sensor, the sensed current peak needs to be at least 100 μA. Moreover, Eureka will cooperate with Prodyne to build a small sensor to cover frequencies of up to 1.4 GHz.

The IP-2 series is a new Line of high frequency current sensors that are used to measure current on small conductors that may be passed through the aperture. Their small size minimizes the physical constraints of usual measurements and the choice of three sensitivities allows for a variety of outputs. The flat response over a wide band is unparalleled compared with similar sensors. A short single ended output with an SMA connector is standard but all models can also be ordered with a differential type output. Modifications to the output length and connector type can be made with little impact to cost.

The relationship between the Sensed current and output voltage is:

$$V_{out} = Z_t \times I \text{ sensed}$$

where Z_t = Transfer Impedance

Electrical specifications of IP-2 Series sensors and its physical configuration are shown in Table 1 and Figure 10 respectively.

Table 1. Electrical Specifications of IP-2 series current probe sensors.

	IP-2-1	IP-2-5	IP-2-10
Freq. range (3 db pts)	100 kHz-1.3 GHz	125 kHz-800 MHz	500 kHz-1 Ghz
Transfer Impedance	1ohm	5 ohms	10 ohms
Current handling cap	0.8 amps (RMS)	0.8 amps (RMS)	0.8 amps (RMS)
Output impedance	50 ohms	50 ohms	50 ohms
Standard connector	SMA	SMA	SMA

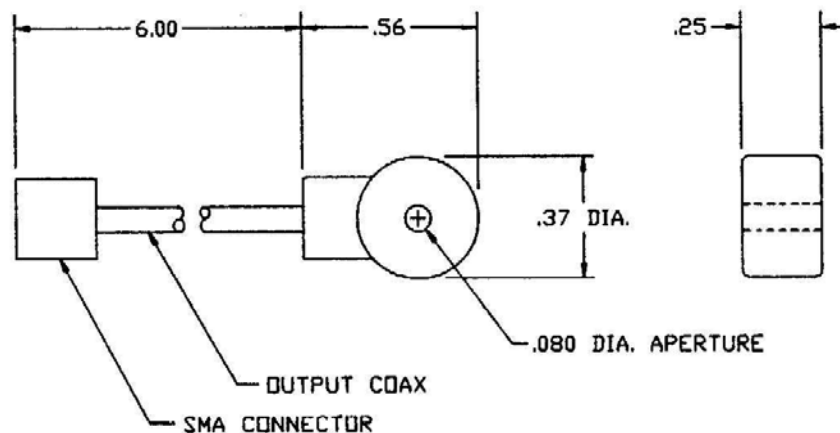


Figure 10. Physical dimensions (in inches) of IP-2 sensor.

Finally, in a transient regime, being a free field sensor, balun (Prodyn Model BIB-120G) was required to be connected to the two outputs of the sensor (not shown above) to provide a suitable coaxial output to measuring equipment.

The test facility (bay) and test vehicles will be provided by the Los Angeles Sheriff's Department (LASD). The tests were carried out for the following six different vehicles

- 2001 Chevy Lumina
- 1996 Ford Taurus
- 1995 Toyota 4Runner
- 1995 Dodge Dakota
- 1998 Nissan Maxima
- 1998 Ford Crown Victoria

where the frequency responses were obtained for key vital engine-related pins/circuits including

- Ignition control
- Ignition coil
- Ignition switch
- Fuel injector
- Injector coil
- Fuel pump relay
- Fuel pump control
- Fuel solenoid valve
- Electronic control module (ECM) relay
- Throttle position sensor
- Automatic shut down relay

- Crankshaft position sensor

Figs. 11 and 12 present illustrative examples showing frequency responses for Dodge Dakota's two critical pins (ignition switch, pin #9 and ignition coil, pin #19).

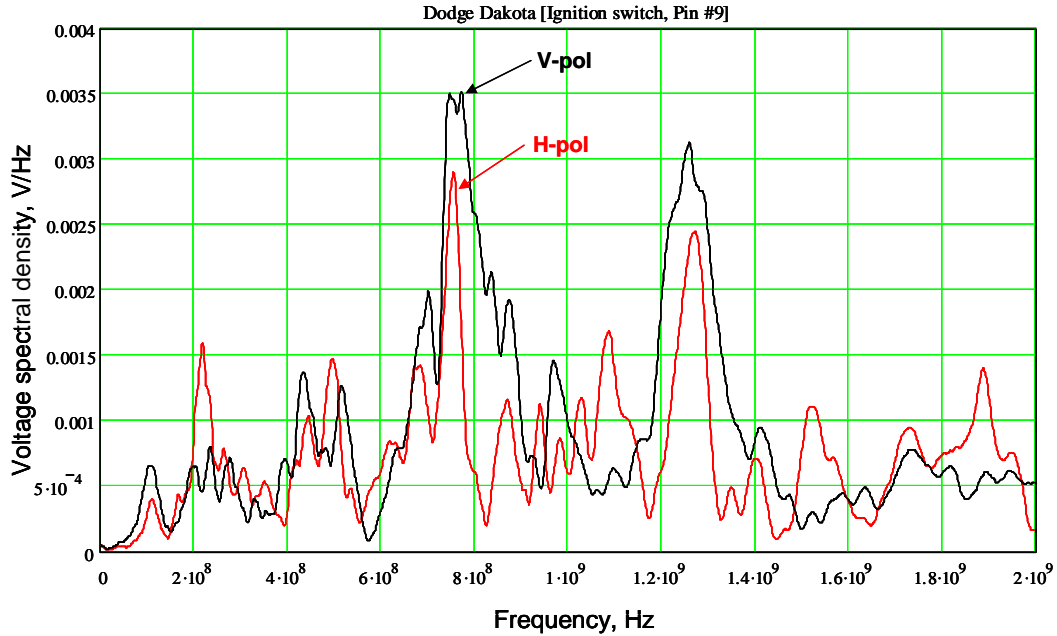


Figure 11. Frequency response for the ignition switch, pin#9 (Dodge Dakota).

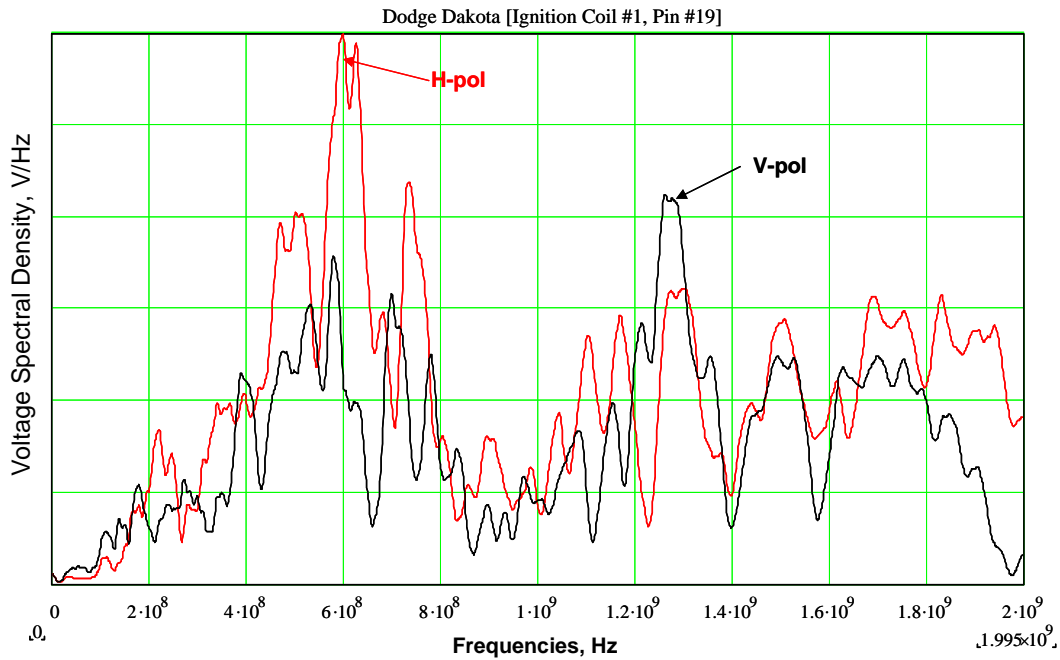


Figure 12. Frequency response for the ignition coil #1, pin#9 (Dodge Dakota).

The frequency vulnerability tests resulted in collection and cataloguing of all vulnerable frequencies in the 200-2000 MHz range for all the above mentioned test cars and the key vital engine functions/pins.

4. Simulations

A numerical model of the Blumlein Oscillator was created and simulated using a Finite Difference Time Domain (FDTD) software.

4.1 Finite Difference Time Domain (FDTD)

In FDTD simulations, a 3-dimensional model is created and divided into 3-dimensional blocks, called Yee cells, a process known as meshing. The model can consist of finite (size) dielectric, electric or magnetic materials. The model exists in a 3-dimensional and finite “solution space”, also consisting of Yee cells. Various boundary conditions can exist on the boundaries of the solution space such as perfect electric conductor (PEC), perfect magnetic conductor (PMC) or absorbing boundary conditions (ABC) the latter of which minimize any reflections at the boundary interface. Once the modeled is created and meshed into the Yee cells and the solution space boundaries are defined, a source is applied and can consist of various different sources such as a uniform plane-wave (UPW) or discrete sources such as voltage sources or current sources, which can vary with time. Once the model, boundaries and excitations are defined, the FDTD process steps through small intervals of time, called time steps, and solves for the electric and magnetic fields at each cell in the solution space, as a function of time. When completed, all electric and magnetic fields are known throughout the solution space, as functions of time, and frequency dependence data can be obtained through the Fourier Transform of the time domain data. Far-fields can also be obtained in post-processing, by using near-field to far-field conversion techniques.

Numerical Model and Simulation

The Blumlein Oscillator was modeled using electric conducting plates with copper conductivity ($5.813 \times 10^7 \frac{S}{m}$). The plates were given a thickness equal to the single Yee cell thickness dimension of 3 mm. A voltage gap-source is placed at each cell along the length of the feeding plate, in order to apply a uniform voltage along the feeding strip edge. 212 discrete voltage gap sources were utilized and were assigned an impedance of 1Ω each. The sources can be seen at the base of the feeding plate, in Figure 15. The time history of the voltage sources was defined by creating a text file with the assigned voltage across each source, as a function of each time-step in the simulation, where each time-step corresponds to 5.778 ps. The voltage across the sources was set to remain at zero for the first few time-steps and then linearly ramp up to 1 volt over a time period of 4 time-steps, to approximate a unit step input while avoiding any sharp discontinuities, which can cause some instability in FDTD.

The 633 mm upper plate terminates into the absorbing boundary condition (ABC) such that no reflections are present due to the finite dimension of this conductive plate in the x-direction. The entire solution space was considered as oil ($\epsilon_r = 2.3$) with the conductivity set to zero such that losses within the oil are not taken into account.

4.2 Simulation Results

The electric field was collected along lines extending in the x-direction at various y and z-locations in the solution space. Because of the meshing of the solution space, each line consists of discrete points spaced 3 mm (cell size) apart. The collection lines begin 1 cell (3 mm), beyond the edge of the lower plate, and run the length (x-direction) of the upper plate to the ABC boundary. In all, 9 collection lines were chosen, 3 at differing heights running along the center of the upper plate, and 6 lines, also at differing heights but running along the edges (in the y-direction) of the upper plate. The average electric field was then filtered (low-pass) to remove some of the high frequency components present. In observing the plot from left to right, the electric field is observed as a function of time at a given observation point. The vertical axis in Figure 13 is the observation point (the point along the averaged lines) such that in observing the plot from bottom to top, the electric field for a fixed time can be noted as the length of the upper plate (in the x-direction) is considered. It can be seen that the electric field is strongest in the region near the first few observation points which is expected due to the close proximity of these points to the lower plate in the geometry.

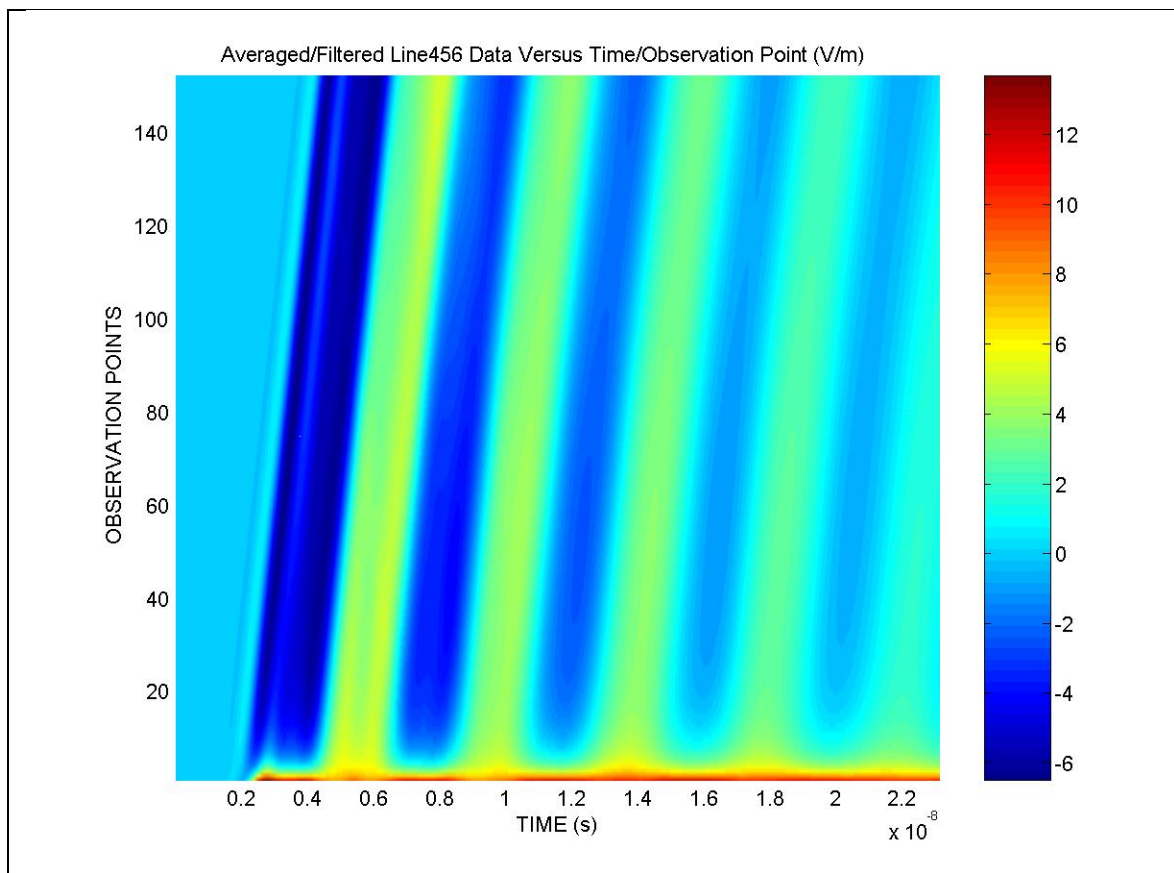


Figure 13. Averaged and filtered electric fields as functions of the observation points and time.

An observation point corresponding to about half the distance down the length of the observation lines were chosen to provide a more detailed analysis of the electric field time history. The point chosen corresponds to observation point 76 from Figure 13. The time history of the electric field was examined at this point along the averaged lines 4, 5 and 6 in order to examine the average electric field in the center of, and halfway down the length of, the upper conductor. The time history of the averaged electric field is shown in Figure 14 both prior to and after the filtering process. Prior to filtering, the high frequency components are visible in the waveform. The filtering process is implemented to remove these higher frequency components. By observing the filtered waveform of the electric field below the top plate, the frequency of operation can be estimated. The average time difference between the peaks in the filtered waveform of Figure 14 is 4.019 ns which corresponds to a frequency of about 248.8 MHz.

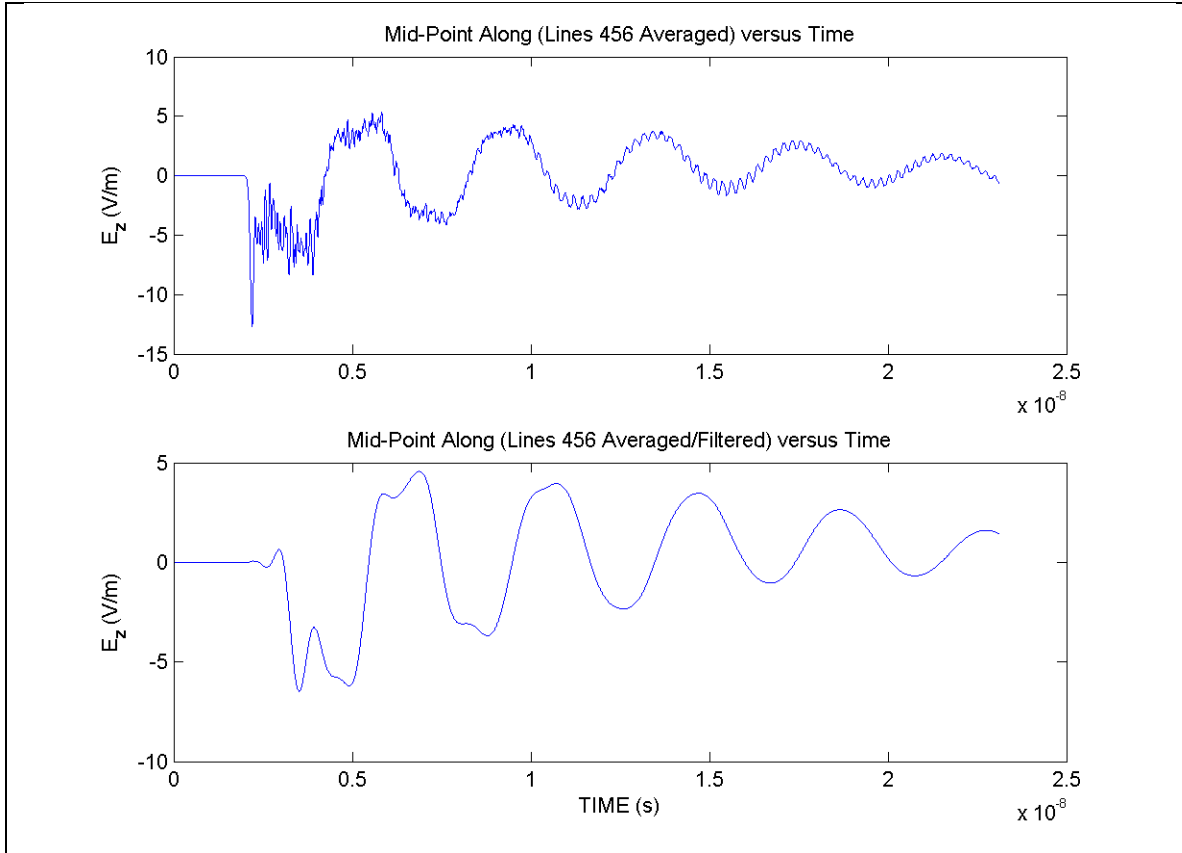


Figure 14. Averaged electric field both before (top) and after (bottom) the low pass filter is applied.

5. High-Power Electromagnetic System (HPEMS)

The picture of the entire high-power microwave system is presented in Figure 15.



Figure 15. The entire fabricated HPEMS.

The major subsystems include:

- The power supply
- Marx generator
- Microwave Oscillator and
- Antenna

The functional system block diagram is shown in Fig. 16. A DC-powered, compact source capable of delivering upwards of 600 kV at 100 Hz, is realized with a 10 kJ/s rapid capacitor charger (APELC Model# PS-RCC-8-10) driving a 16 stage Marx generator (APELC Model# MG16-3C-2700PF).

5.1 Power Supply

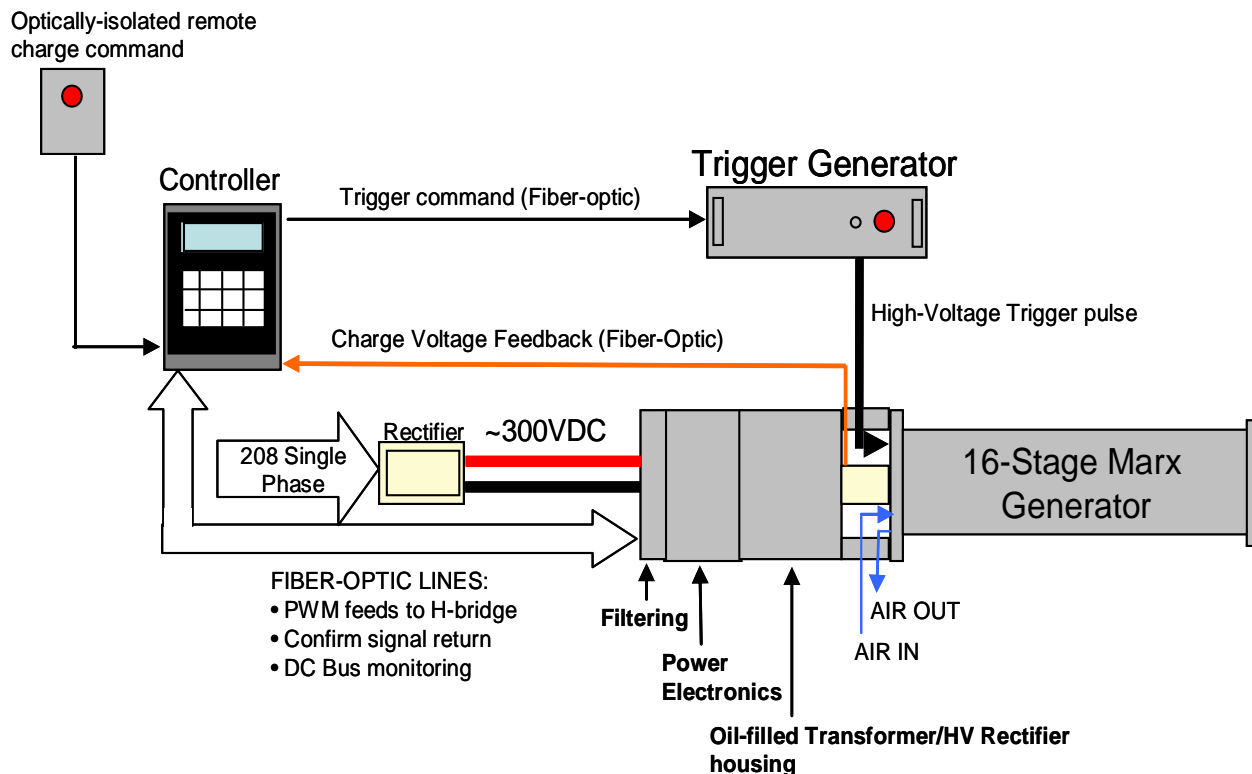


Figure 16. 600 kV, 100 Hz compact source (power supply and Marx generator).

PS-RCC-8-1 Rapid Capacitor Charger

The Marx generator is charged in less than 10ms by the APELC PS-RCC-8-1 Rapid Capacitor Charger. The charger employs a *Freescle 9S12* processor to coordinate two channels of Pulsed-width Modulated (PWM) signaling, driving the gates of an IGBT-switched H-Bridge. The processor of the 9S12 runs at 24 MHz, allowing ample duty-cycle resolution at a switching frequency of 30 kHz.

Charging Cycle

The controller (Fig. 17 and Fig. 18) for the high-voltage source provides a user interface for setting the number of shots, charge voltage, and the auto-shutdown function, while handling all the major timing and PWM signals for the charger and trigger generator. The controller is self-contained inside of a metal enclosure and operates the charger via fiber-optic lines, providing shielding and isolation from high radiated field strengths. The five fiber-optic control lines are as follows:

1. **Drive A:** Drives the gates of one of the diagonal pairs of IGBT's in the H-bridge.
2. **Drive B:** Drives the gates of the other diagonal pair.

3. **Confirm:** Indicates that only one diagonal of the H-bridge is driven, the drive signal is received properly, and no error signal exists from the IGBT drivers.
4. **DC-Bus:** Optically isolated voltage monitoring of the DC-Bus, viewable from the digital display of the controller.
5. **Feedback:** Monitors the voltage output (charging voltage) of the charger. The voltage is sent back in real time as a train of pulses, the frequency of which increases with the voltage. This allows the maximum charge voltage to accurately match the voltage set on the controller display with a high degree of shot-to-shot stability.

During a typical charging cycle, the user switches on the power to the DC bus, sets the number of shots and charge voltage on the controller's keypad, and closes the lid; ensuring proper shielding. Once all of these conditions are set, the user activates the charging/firing cycle by pressing a momentary switch located on a separate, fiber-optically isolated remote. This action sends the command to the microcontroller to begin charging.

The PWM signal to the H-bridge is generated from look-up tables stored in memory on the 9S12 microcontroller. These tables allow the charger to throttle-up the PWM as quickly as possible without generating an over-current condition on the IGBT's. If an over-current condition occurs due to any event during charging, a fault condition is sent to the controller, and the PWM signal is stopped immediately. Otherwise, the driver sends the pulses to the H-bridge until the microcontroller detects that the preset charge voltage has been achieved. The controller then ceases PWM generation and transmits a pulse, again via fiber-optic, to the trigger generator. After the trigger pulse is sent, the controller gives the maximum amount of blanking time for a 100Hz pulse-repetition frequency and then begins the charging sequence again (unless only one shot has been specified).

Power Electronics, Transformer, and Rectifiers

Pictured in Figure 17 is the PS-RCC-8-1 Rapid Capacitor Charger removed from its housing. The power-electronics and high-voltage assembly are separated by an aluminum plate that serves as a bulk-head isolating the oil section from the open air, as well as providing a heat-sink for the IGBT's. The DC power connects directly to the H-bridge board and is buffered by the cylindrical capacitors located below the IGBTs, providing 360 J's of energy storage on the DC bus. The IGBTs switch the DC bus, generating a 30 kHz PWM waveform directly to the primary of the *Stanganes* high-frequency step-up transformer. The transformer outputs to the epoxy-potted rectifiers through a total of 12 taps, providing extra hold off for the transformer and the rectifiers. The high-voltage DC is then fed through a 1k Ω carbon resistor (not pictured) to an output connector coupling into the Marx generator.

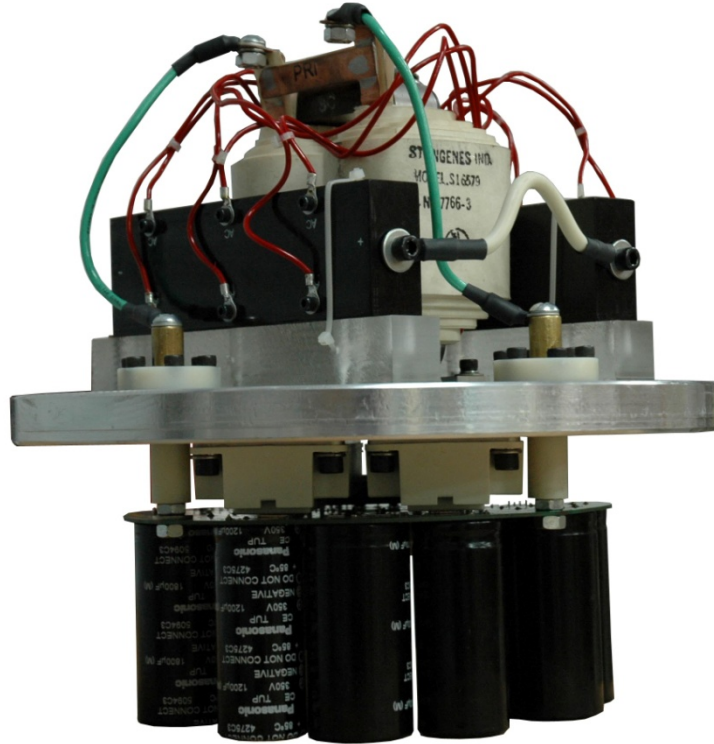


Figure 17. PS-RCC-8-1 Rapid Capacitor Charger.

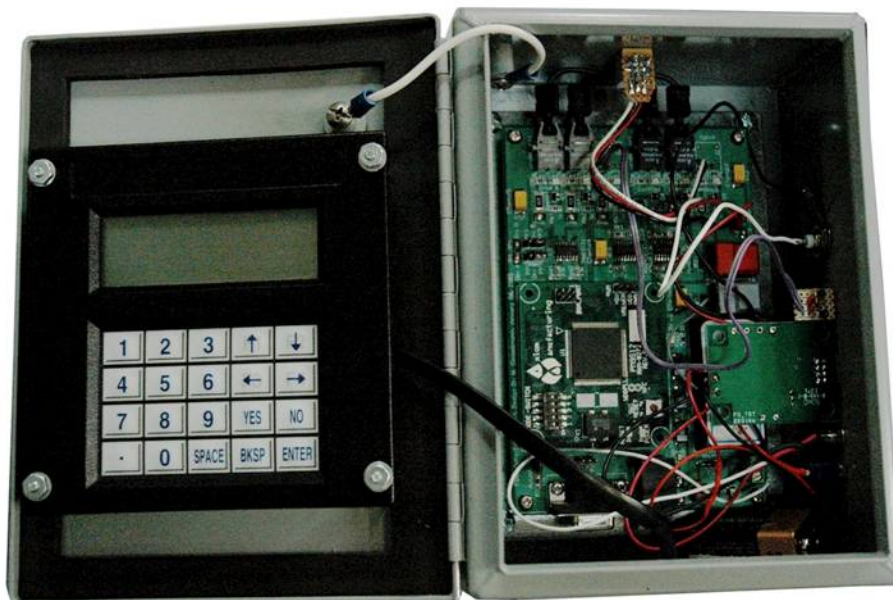


Figure 18. Charger controller (open).

5.2 Trigger Generation and Marx Generator

The PS-RCC-8-1 provides 10 kJ/s at 40 kV to a MG16-3C-2700PF 16-stage Marx generator. Table 2 shows the specifications for the generator.

Model:	MG16-3C-2700PF
■ Physical Specs:	42 inch length, 8 inch diameter, 75 lbs
■ Charge voltage:	10 - 40 kV
■ Erected voltage:	160 - 640 kV
■ Internal impedance:	23 Ohms
■ Peak power:	2 GW
■ Stored Energy:	~100J at 40kV charge
■ Minimum charge time:	5 ms (power supply dependent)

Table 2. APELC's MG16-3C-2700PF Compact Marx Generator.

The Marx generator (see Fig. 19) utilizes inductive charging elements to allow for fast charge times and the elimination of component failure associated with resistive charging. Once charged, the Marx is triggered by a 30 kV pulse applied to the first stage by a thyatron based trigger generator. As discussed previously, the trigger generator receives an optical trigger pulse from the controller unit (see Fig. 16) at the precise moment the controller detects that the generator has reached the preset charge voltage. By utilizing the maximum time between charge cycles and a constant flow of dry air to the spark gaps, the Marx generator is able to stably achieve a 100 Hz pulse repetition frequency.



Figure 19. Marx generator and power supply.

5.3 Blumlein Microwave Oscillator

The oscillator subsystem (Fig. 20) converts 640 kV DC pulses from the Marx generator into microwaves at a specified frequency, which is controlled by the Blumlein length. The oscillator consists of the transfer capacitor (plate on the right side), matched to the erected capacitance of the Marx generator, which we charge before the energy transfer to the Blumlein. Once it is charged to the specified charging voltage (640 kV), which takes approximately 30-35 ns, the transfer capacitor switches close thus commencing the Blumlein charging process, which takes approximately 4 ns. When Blumlein (left plate) is fully charged, then the multiple Blumlein spark-gap switches close rapidly causing the voltage wave go back and forth along the Blumlein causing oscillations and being radiated into space via the load (antenna).



Figure 20. Flat plate Blumlein configuration oscillator subsystem.

5.4 Antenna

The antenna subsystem utilized during the effort is essentially a flare horn antenna, whose gain at 350 MHz is estimated to be approximately 10 dBi. Figure 21 shows



Figure 21. Flare horn antenna subsystem

two antenna pictures: side view (top) and front view (bottom). At 350 MHz for this antenna we have the following relationship between the radiated electric field, the voltage and the range:

$$E \sim 1.07 \frac{V}{r} .$$

For example when $V=640$ kV, at 10 m range we have $E \sim 68$ kV/m.

6. High-Power Microwave Experiments

6.1 Test Design and Test Configuration.

The experiments were conducted in Eureka's microwave laboratory throughout the duration of the effort. Initially, the testing was done using a simple workable model with a relatively simple Blumlein switch configuration. Later, the oscillator system was refined to yield better switching system and more advantageous oscillator. Further refinements of the power supply system and newly designed switch configuration utilizing Elkonite electrodes for both the transfer capacitor and the Blumlein yielded the final system architecture.

In order to assess the system performance, we utilized multitude of B-dot and D-dot sensors. They D-dot sensor placed under the transfer capacitor was utilized for assessing the transfer capacitor charging process and the breaking of the transfer capacitor switches, while D-dot sensors placed near Blumlein rail were measuring Blumlein charging and closure of its switches. Finally, B-dot sensor at the distance was measuring free-space magnetic flux through the sensor loop, which after integrating was converted to a free-space electric field - the key parameter for assessing the HPEMS performance.

All the measured signals were recorded by 4 Channel TDS 7404 Digital Scope. Simultaneous measurements were done for each data take to assure that the absolute and relative timings of each event were evaluated and assessed.

To contain large radiated fields, the HPEMS was placed inside a 24X12ft Faraday cage, while the measuring scope and the computer were placed outside the Faraday cage. Special filtering provisions were made to assure no interference induced on connecting cables and wires. The exception was during the tests against actual vehicles, in which case the HPEMS was placed outside the Faraday cage facing the bay doors (towards the vehicle) of the microwave lab, while the equipment was placed inside the Faraday cage.

6.2 Electric Field Measurements

The electric field measurements were carried out using a B-dot sensor. The B-dot sensor Model B90-R and Balun Model BIB-100G were acquired from Prodyn Technologies, Albuquerque, NM to measure the magnetic field flux and then to convert it into the electric field. The values of the received voltage and the electric field were calculated using the measured values of $\frac{\partial B}{\partial t}$ with B-dot sensor. Then, the measured values of $\frac{\partial B}{\partial t}$ were converted to the values of the electric field using the following method. The value of voltage at the sensor output relates to the value of $\frac{\partial B}{\partial t}$ by:

$$V_s(t) = A_{eq} \frac{\partial B}{\partial t},$$

where A_{eq} is the sensor's equivalent area. Since the measured voltage, V_m , is proportional to the sensor voltage, V_s , we have,

$$V_m(t) = kV_s(t) = kA_{eq} \frac{\partial B}{\partial t} = k \frac{A_{eq}}{c} \frac{\partial E}{\partial t},$$

where k is a constant of proportionality (due to sensor attenuator value), $c = 3 \times 10^8$ m/sec is the speed of light in vacuum, and we used the fact that $E = cB$. Then it follows that,

$$E(t) = \frac{c}{kA_{eq}} \int_0^t V_m(t') dt'.$$

Taking the values $A_{eq} = 10^{-5}$ and $k = 0.8$ (sensor's Balun attenuator) it follows that,

$$E(t) = 3.75 \times 10^{13} \int_0^t V_m(t') dt'.$$

6.3 Test Results

The Figs. 22-24 illustrate the results of the measurements associated with the key elements of the system, including the temporal profiles of the transfer capacitor and Blumlein charging and switching, while Fig. 24 presents the resulting radiated electric field measured at 30-ft range from the antenna.

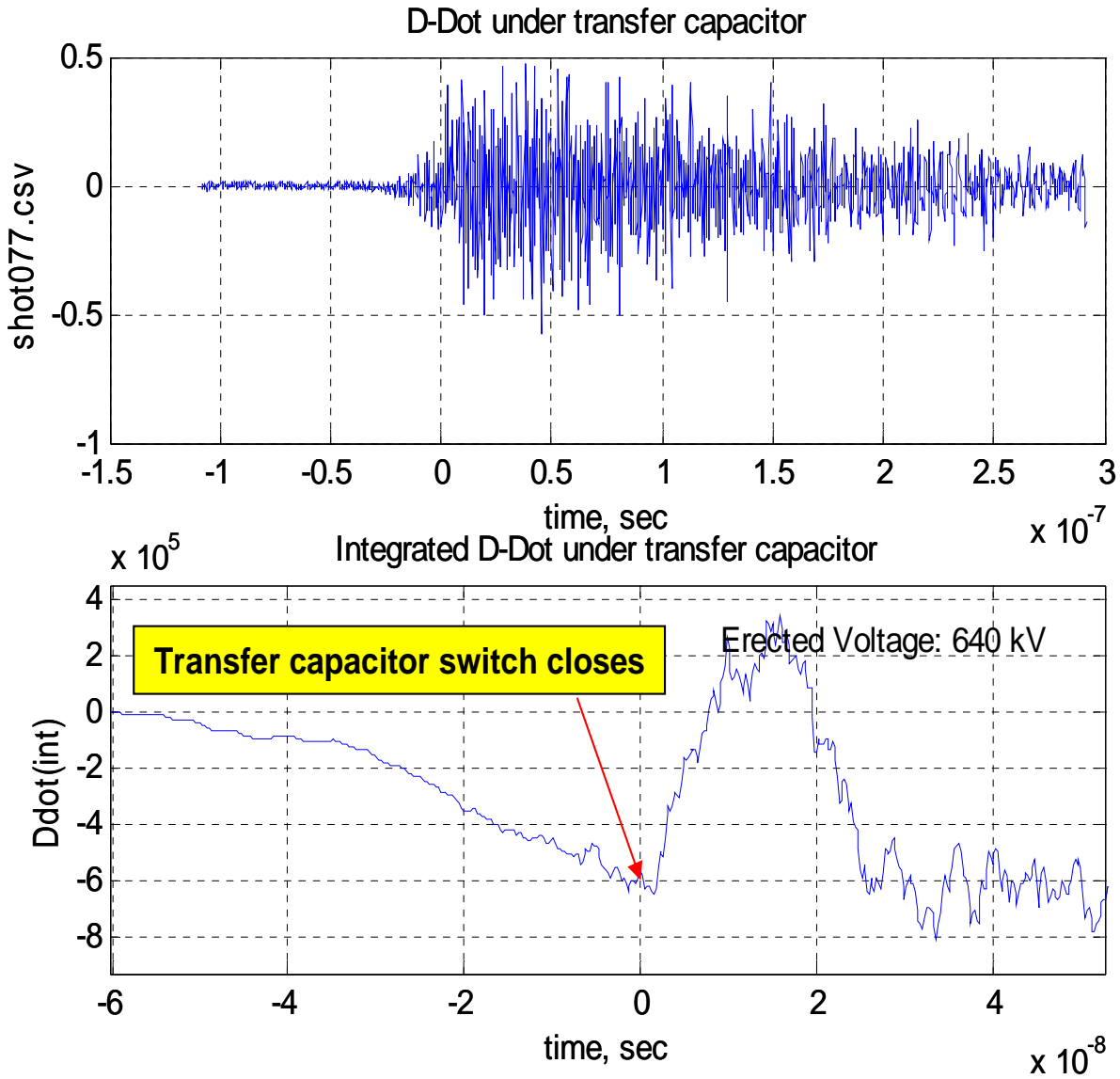


Figure 22. Measured D-Dot signal and charging of transfer capacitor.

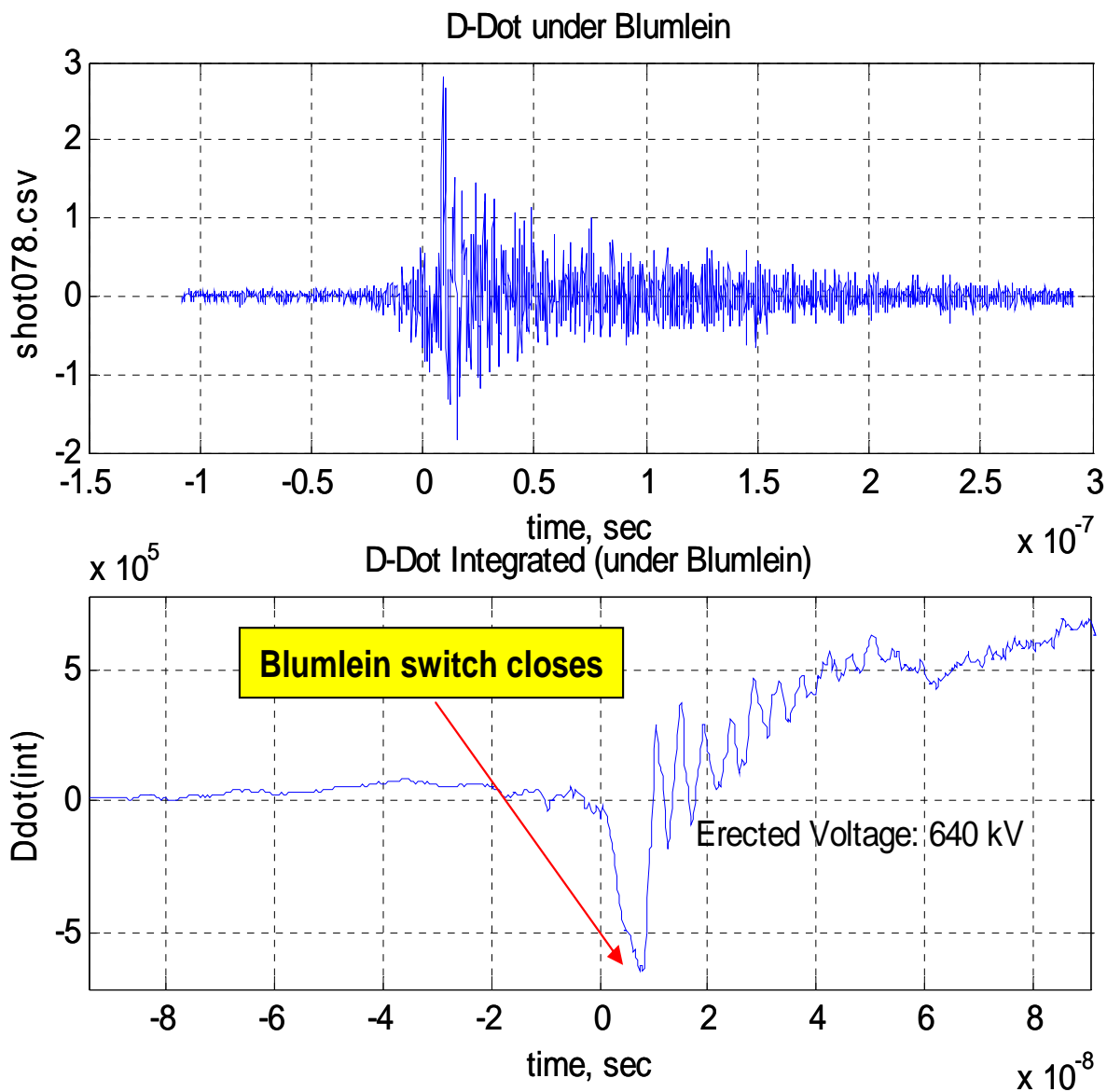


Figure 23. Measured D-Dot signal under the Blumlein.

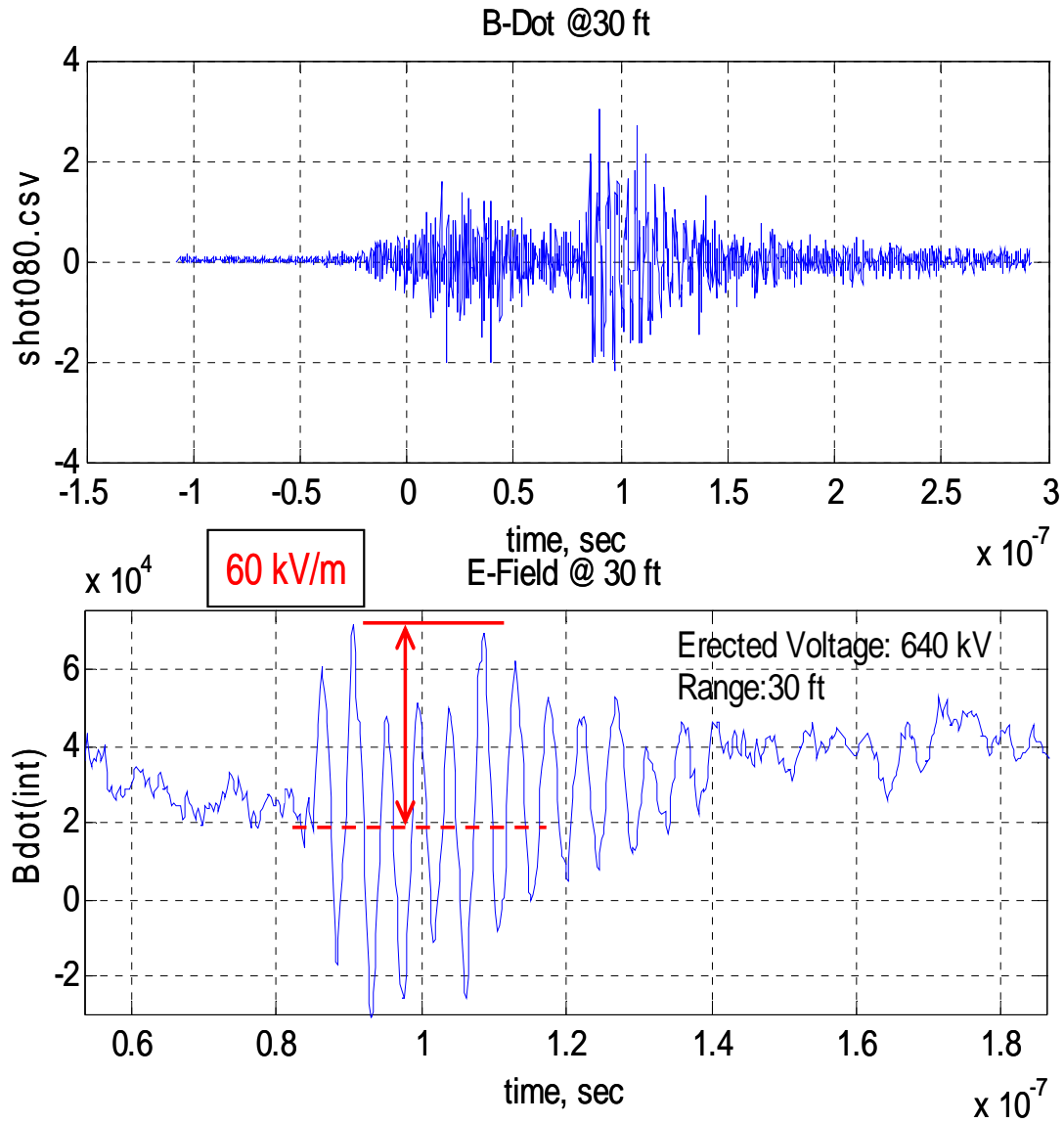


Figure 24. Measured D-Dot signal and electric field @ 30 ft from the antenna.

7. Summary

Eureka Aerospace has developed a high-power electromagnetic system (HPEMS) for remotely immobilizing vehicles using microwave energy to disable/damage vehicle's electronic control module/microprocessors which control engine's vital functions. The system is capable of (1) high-value asset perimeter protection from approaching hostile vehicles, (2) bringing cars to halt on urban, suburban roads and multi-lane highways, (3) perimeter protection for gas-oil (fueling) platform at sea and (4) day/night, all weather clandestine operations.

HPEMS consists of 3 major elements:

1. Power Supply and Marx generator
2. Tunable RF Oscillator
3. High-gain antenna

The power source consists of 16-stage Marx generator having erected voltage of 640 kV, generating high energy (103 J each) pulses at PRF=100 Hz, yielding 10 kW average power. Marx generator is being fed a 40 kV (max) charging voltage from the power supply operating at maximum 100 Hz PRF. In the future, the design goal is to achieve PRF=1000 Hz, thus increasing the average power by 10 dB.

The Marx generator is charged in less than 10ms by the APELC PS-RCC-8-1 Rapid Capacitor Charger. The charger employs a *Freescale* 9S12 processor to coordinate two channels of Pulsed-width Modulated (PWM) signaling, driving the gates of an IGBT-switched H-Bridge. The processor of the 9S12 runs at 24 MHz, allowing ample duty-cycle resolution at a switching frequency of 30 kHz. The controller for the high-voltage source provides a user interface for setting the number of shots, charge voltage, and the auto-shutdown function, while handling all the major timing and PWM signals for the charger and trigger generator. The controller is self-contained inside of a metal enclosure and operates the charger via fiber-optic lines, providing shielding and isolation from high radiated field strengths.

The prototype microwave oscillator consists of a two-plate transmission line Blumlein configuration and a fast (less than 500 ps) closing multiple spark-gap switches, which traps the pulses between the switches and the antenna (load) and thus converts Marx's dc energy into microwave energy at a frequency controlled by the length of the transmission line.

An auxiliary transfer capacitor is utilized as an intermediated energy storage device which is charged in less than 40 ns and then quickly (4-5 ns) discharged onto Blumlein, yielding very efficient energy transfer from Marx generator to the Blumlein oscillator.

High-gain antenna constitutes an integral part of the oscillator, since it represents the load of the oscillator circuit. Its terminals are connected to the transmission line and it radiates due to the oscillating voltage on its terminals. In the development of antenna subsystem, the key elements are: (1) suitable impedance allowing for efficient radiation and yet

permitting adequate oscillations to occur between the switch and antenna for having large Q, (2) antenna size and shape for achieving required gain and yet not be obtrusive. Currently, flare horn antenna consisting of diverging copper tubes is utilized to yield an approximately 10 dBi gain. The other candidate antennas include spiral antenna and an impulse radiating antenna (IRA). Current system has only VV-polarization; the future operational system will employ both H and V. Utilization of a circularly polarized fields using a suitable antenna appears to be a viable option.

Eureka Aerospace carried out a series of so-called “vulnerable” frequencies tests to evaluate the resonances in the vehicles’ microprocessors circuits associated with the most vital engine functions, such as ignition control, fuel pump control etc. This was done by measuring frequency response for each circuit/pin inside the vehicles’ Electronic Control Module (ECM). Test vehicles included US and foreign manufacturers such as Ford, GM, Chrysler Daimler, Toyota, Nissan and Honda. This process led to the identification of the “bank” of “vulnerable” frequencies in the 200-1350 MHz range. We strongly believe that using these specific frequencies will lead to the optimal high-power microwave system, requiring relatively smaller power-aperture product to achieve the desired goal of disrupting and/or damaging the microprocessors. This, in turn will yield more compact, lightweight system.

Microwave oscillator together with a high-power switch constitutes an integral part of the entire HPEMS. The current prototype system operates at a single frequency; the objective optimal system will employ a tunable oscillator capable of generating microwaves in the 200-1350 MHz range. The choice of a dielectric medium inside the switch, which will be based on the magnitude of the maximum voltage on its electrodes, the size of the gap between electrodes together with antenna impedance, is selected to achieve the most efficient power transfer from Marx generator to the radiating antenna. Moreover, to accommodate large voltages, the switch multi-channeling is achieved, which significantly reduces the parasitic inductance of the switch.

The initial test results were very encouraging: the prototype was shown to deliver an approximately 60 kV/m at 30 ft range from the antenna and to “kill” the engine of 1999 Honda Accord using a single radiated pulse. More tests employing wide range of HPEMS/target-related parameters is warranted for a reliable assessment of the prototype HPEMS.

Finally, to avoid collateral damage to other vehicles, particularly on multi-lane highways, HPEMS is designed to optimize the antenna beam size, given operational frequency and the limitations of the antenna aperture size, which, together with system operational procedures (distance to the target vehicle and aspect angle) will assure the “illumination” of the target vehicle only.

The overall prototype HPEMS is compact and weighs approximately 230 lbs and can be integrated into a police car (Ford Crown Victoria) with the following operational capabilities. Further reduction in system size and weight are feasible.

References:

- [1] W. Prather, C. Baum et al. "Ultra-wideband Source and Antenna Research". IEEE Trans. Plasma Sci., Vol.28, pp. 1624-1630, Oct. 2000.
- [2] R. Barker and E. Shamiloglu. High-Power Microwave Sources and Technologies. IEEE Press, New York, 2001.
- [3] W. Prather et al. "Survey of Worldwide Wideband Capabilities" IEEE Trans. on EMC; Special Issue on International EMI, Aug 2004.
- [4] D. Giri and C. Baum. "Temporal and Spectral Radiation on Boresight of a Reflector Type of Impulse Radiating Antenna (IRA)", in Ultra-Wideband, Short-Pulse Electromagnetics 3, C. Baum, L. Carin and A. Stone, Eds. New York Plenum, pp. 65-72, 1997.
- [5] S. Tyo, M. Skipper et al. "Frequency and Bandwidth Agile Pulser for Use in Wideband Application". IEEE Trans. Plasma Science, Vol.32, N0.5, Oct. 2004.
- [6] J. Schoenberg, J. Burger, S. Tyo et al. "Ultra-wideband Source Using Gallium Arsenide Photoconductive Semiconductor Switches", IEEE Trans. Plasma Sci., Vol.25, pp.327-334, April 1997.
- [7] G. Staines. "Compact Sources for Tactical RF Weapons Application". DIEHL Munitionssysteme. Amerem-2002, Maastricht, Netherlands, 2002.
- [8] D. Giri. "JOLT: a Highly Directive, Very Intensive, Impulse-like Radiator". Sensor and Simulation Notes #480. Albuquerque, NM; Air Force Research Lab, 2003.
- [9] M. Berry M. 1997. Electrical Vehicle Stopper Evaluation: TRW. Army Research Laboratory Report ARL-TN-89, April, 2004.
- [10] J. Tatoian "Modeling of RF Tunable Source Performance" SBIR Phase II Progress Report #10, Submitted to MARCORSYSCOM, November 29.
- [11] D. Helmick. "Assessment of Cooperative Technologies for Terminating Pursuits". California Highway Patrol, Office of Special Projects Report, October 1, 2001.
- [12] K. Bayless and R. Osborne. "Pursuit Management Task Force Report". Final Project Report. U.S. Department of Justice. September 1998.
- [13] J. Tatoian "MP Vulnerable Frequencies Test Configuration "SBIR Phase II Progress Report #2, Submitted to MARCORSYSCOM, March 11, 2004.